University of Thessaly
School of Engineering
Department of Mechanical Engineering

A modified boundary layer formulation for the problem of Mode-I loading of the single-edge notched specimen in a hydrogen environment.

by

GIANNOULAS KONSTANTINOS

Submitted in partial fulfillment of the requirements for the degree of
Diploma in Mechanical Engineering at the University of Thessaly
Volos, 2025

University of Thessaly
School of Engineering
Department of Mechanical Engineering

A modified boundary layer formulation for the problem of Mode-I loading of the single-edge notched specimen in a hydrogen environment.

by

GIANNOULAS KONSTANTINOS

Submitted in partial fulfillment of the requirements for the degree of
Diploma in Mechanical Engineering at the University of Thessaly
Volos, 2025

Approved by the Committee on Final Examination:

Supervisor

Professor Nikolaos Aravas
Department of Mechanical Engineering, University of Thessaly

Member

Professor Gregory N. Haidemenopoulos
Department of Mechanical Engineering, University of Thessaly

Member

Associate Professor Michalis Agoras
Department of Mechanical Engineering, University of Thessaly

Date Approved: [June 18, 2025]

Acknowledgements

The present thesis was carried out in partial fulfilment of the requirements for the Diploma in Mechanical Engineering at the Department of Mechanical Engineering of University of Thessaly.

First and foremost, I want to thank my parents, Ariadni and Ioannis for their support since my first steps until now. They always pushed me to reach where I thought I never could and for their valuable, unconditional trust and love, I will always be thankful. For being there for me and for always supporting me while chasing my dreams, they have my deepest gratitude.

Next, I want to thank my diploma thesis supervisor, Professor Nikolaos Aravas. Through his excitement about the field of his expertise, I also got intrigued by the field of solid mechanics. I will always be thankful for trusting me and helping me fulfil my dreams. His ethics and personality will always be an inspiration for me, as it will always be an honour of mine to have cooperated and learned alongside a professor like him.

I also want to thank the members of the advisory committee, Professor Gregory Haidemenopoulos and Associate Professor Michalis Agoras for the valuable time they devoted in reviewing this thesis.

Next, I am thankful to Dr. Sokratis Xenos for assisting and guiding me through the process of conducting my research either it was learning how to use the FEA software ABAQUS or pointing out my mistakes and giving me the chance to develop as a researcher. His advices and comments have always been helpful.

Last but surely not least, I want to thank my friends. I could not have been any luckier and the healthy competition we had amongst us since day one at the university pushed me to be better in order to compete with you. You will all have a special place in my heart and without you these past five years would not have been the same.

To all that trusted me, to all that believed in me: Thank you!

A modified boundary layer formulation for the problem of Mode-I loading of the single-edge notched specimen in a hydrogen environment.

GIANNOULAS KONSTANTINOS

Department of Mechanical Engineering, University of Thessaly

Supervisor: Professor N. Aravas

Abstract

In this work, a modified boundary layer formulation is used for the prediction of the mechanical and hydrogen fields developing near the crack tip of the Single Edge Notch Tension (SENT) specimen loaded in plane strain tension. The effect of the so called "T-stress" is accounted for in the numerical calculations. Transient diffusion and trapping/detrapping kinetics are also considered. A coupled mechanical-diffusion model is implemented in ABAQUS/Standard via the provided UMAT and UMATHT user-subroutines by taking advantage of a thermo-mechanical analogy. Comparison between the boundary layer formulation and the full-field results from the SENT specimen reveal reasonable agreement in both the mechanical fields and the hydrogen distribution in the vicinity of the crack tip.

Contents

List of Figures

List of Tables

Introduction

It is not rare for an application to demand a steel component to function in a hydrogenous environment. It has been observed though, through the years, that such components might fail in sub-critical loading. The reason why this occurs, is that the atoms of the gaseous hydrogen diffuse in the metal's lattice affecting its microstructural integrity. Hence, the mechanical properties of the material downgrade and it becomes more brittle. This phenomenon is called Hydrogen Embrittlement (HE). Some factors that boost the gas's diffusion, are the temperature and the pressure the gas applies on the metal.

In order to predict the mechanical and hydrogen distribution fields developing at the vicinity of an axial crack in a pipeline steel, the SENT specimen can be used as suggested by Dadfarnia et al. (2011) [7]. Also, based on [8], a modified boundary layer formulation accounting for the effect of the so called "T-stress" has to be used, in order to accurately predict the stress state at the crack tip. The boundary layer formulation can serve as an efficient methodology for such predictions with reduced computational cost compared with the full field calculation. In this regard, the appropriateness of using a boundary layer formulation is investigated, for the prediction of the stress and hydrogen fields ahead of a crack tip in comparison with calculations carried out in the actual SENT specimen.

In Chapter 1, the theory of hydrogen diffusion is described. The forms by which hydrogen can be found in the metal's lattice and how its concentration can be estimated are examined. Also, the elastoplastic equations that characterise the material's behaviour are presented, in order to calculate the mechanical fields that are developed due to external loading. Elements from the theory of fracture mechanics are briefly recalled, since the problem under examination includes a crack opening and the stress fields at its tip must be estimated.

Chapter 2, deals with the description of the details regarding the simulation set-up. The boundary and initial conditions are discussed along with the analogy made between the mass diffusion and heat transfer, since ABAQUS can not simulate coupled mass transfer - stress analysis problems, unless user-defined finite elements are developed. To avoid possible numerical instabilities due to the discrepancy among the magnitudes of the coupled mechanical and diffusion equations, all the quantities were normalized as explained. The predictions from the numerical simulations are compared to some available results from the simulations of the corresponding SENT specimen.

Standard notation is used throughout. Boldface symbols denote tensors the orders of which are indicated by the context. All tensor components are written with respect to a fixed Cartesian coordinate system with base vectors $\mathbf{e}_i$ $(i = 1, 2, 3)$, and the summation

convention is used for repeated Latin indices, unless otherwise indicated. The prefice det indicates the determinant, a superscript T the transpose, a superposed dot the material time derivative, and the superscripts sym and $skew$, enclosed in parentheses, the symmetric and anti-symmetric parts of a second order tensor. Let $\mathbf{a}$, $\mathbf{b}$ be vectors, $\mathbf{A}$, $\mathbf{B}$ second-order tensors, and $\boldsymbol{\mathcal{C}}$, $\boldsymbol{\mathcal{D}}$ two fourth-order tensors; the following products are used in the text: $(\mathbf{a}\,\mathbf{b})_{ij} = a_i\, b_j$, $\mathbf{A} : \mathbf{B} = A_{ij}\, B_{ij}$, $(\mathbf{A}\cdot\mathbf{B})_{ij} = A_{ik}\, B_{kj}$, $(\mathbf{A}\,\mathbf{B})_{ijkl} = A_{ij}\, B_{kl}$, $(\boldsymbol{\mathcal{C}} : \mathbf{A})_{ij} = \mathcal{C}_{ijkl}\, A_{kl}$, and $(\boldsymbol{\mathcal{C}} : \boldsymbol{\mathcal{D}})_{ijkl} = \mathcal{C}_{ijpq}\, \mathcal{D}_{pqkl}$. The inverse $\boldsymbol{\mathcal{C}}^{-1}$ of a fourth-order tensor $\boldsymbol{\mathcal{C}}$ that has the "minor" symmetries $\mathcal{C}_{ijkl} = \mathcal{C}_{jikl} = \mathcal{C}_{ijlk}$ is defined so that $\boldsymbol{\mathcal{C}} : \boldsymbol{\mathcal{C}}^{-1} = \boldsymbol{\mathcal{C}}^{-1} : \boldsymbol{\mathcal{C}} = \boldsymbol{\mathcal{I}}$, where $\boldsymbol{\mathcal{I}}$ is the symmetric fourth-order identity tensor with Cartesian components $\mathcal{I}_{ijkl} = (\delta_{ik}\,\delta_{jl} + \delta_{il}\,\delta_{jk})/2$, δ_{ij} being the Kronecker delta.

Chapter 1

Theory

In this chapter the constitutive equations for the diffusion and mechanical problem are presented. Also, the process of numerical integration is being explained, in order to fully present the process ABAQUS follows when calculating the quantities of interest in each time increment. A brief outline of the Mode-I asymptotic solution from the theory of fracture mechanics is also given here for convenience.

1.1 Theory of hydrogen

When a steel component comes in contact with gaseous hydrogen, at some occasions atoms might diffuse in the metal's lattice. These solute atoms change the chemical potential of the matrix, since they intervene to its integrity and due to the dilation of the lattice that they cause, internal, localized stresses are introduced. Hydrogen can either diffuse through Normal Interstitial Lattice Sites (NILS) or be trapped at micro-structural defects (e.g., grain boundaries, voids, precipitates etc.) that exist in the material's micro-structure. The reason why hydrogen migrates through the material, is the mechanics of diffusion. The solute atoms have the tendency to move from regions with higher chemical potential to those with lower one [9, 10]. Apart from that, since the applied mechanical loads are not negligible, a yield criterion should be chosen and the respective equations from the field of fracture mechanics must be expressed.

After some extensive analysis was conducted, it was observed that the mechanical properties of steel components functioning in an environment containing hydrogen downgrade significantly, especially their strength and ductility [5]. This degradation of the material's properties can lead to sub-critical crack growth, occasionally leading to catastrophic failure. What affects the behaviour of the material, is the diffusion of atomic hydrogen into the metal's micro-structure [4] since the atoms migrate through the lattice and might eventually get trapped at some existing micro-structural defects [7]. This intervention to the material's integrity can lead to failure, even when the applied stress is less than the maximum stress the application was designed to withstand [3]. The degree at which hydrogen affects the metal can be influenced both from the amount of the hydrogen atoms that are absorbed

in the metal's lattice and the micro-structure of the material [6], along with the environment's temperature and the pressure the gas applies [1], [2]. This phenomenon is known as Hydrogen Embrittlement (HE) and is notorious for its impact on the ductility and fracture resistance of the material in question.

1.1.1 Hydrogen transport

All real solids contain imperfections in their lattice, such as voids, impurities and dislocations and such defects are possible traps for the hydrogen atoms [12]. It has been proven, that the hydrogen concentration in trapping sites influences the stress at which a crack will propagate. Furthermore, the traps are considered either reversible, when the required energy for hydrogen atoms to escape has a small magnitude, or irreversible, when the atoms need to obtain a lot of energy to be released from the trapping sites [13]. These trapping sites partially prevent further hydrogen diffusion and their concentration of hydrogen atoms can be estimated as

$$C_T = \theta_T N_T, \quad N_T(\bar{\varepsilon}^p) = 10^{f(\bar{\varepsilon}^p)} \tag{1.1}$$

with C_T being the concentration measured in trapped hydrogen atoms per unit of volume, N_T expresses the trap density in traps per unit volume and is a function of the local equivalent plastic strain $\bar{\varepsilon}^p$, which will be defined in the following and θ_T is the occupancy of the trapping sites in the lattice.

As suggested by Kumnick and Johnson (1980) [21] the trap density N_T and the equivalent plastic strain $\bar{\varepsilon}^p$ relate to each other in such way, that when $\bar{\varepsilon}^p$ reaches a specific value, the magnitude of N_T remains practically constant, reaching a trapping saturation, as shown in Fig. 1.1.

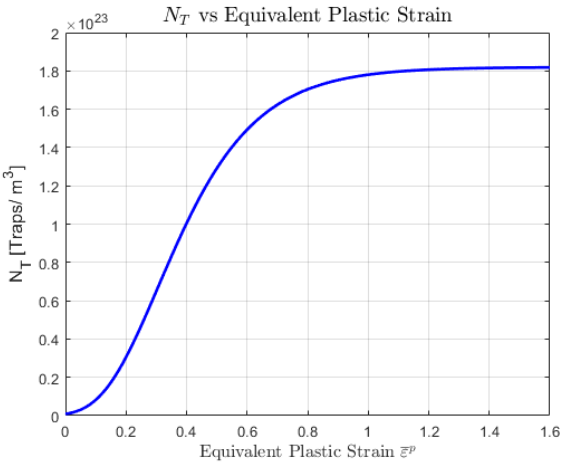

Figure 1.1: Trap density, N_T as a function of equivalent plastic strain $\bar{\varepsilon}^p$ [21].

Apart from the trapped atoms, hydrogen can be found in NILS, which are points in the lattice that the hydrogen atoms can migrate through. These sites can be overcome from the atoms with less energy than the trapping sites. The concentration of C_L, measured in

hydrogen atoms per unit volume is expressed as

$$C_L = \theta_L N_L \tag{1.2}$$

where θ_L is the occupancy of the interstitial sites and N_L denotes the number of solvent atoms per unit volume. Also, since $N_A = 6.02214076 \times 10^{23}\,\text{mol}^{-1}$ is the Avogadro's number and V_M is the molar volume of the host lattice estimated in units of volume per mole, N_L can be estimated as $N_L = \frac{N_A}{V_M}$. In conclusion, hydrogen can be found in the matrix in two ways, either migrating through NILS or trapped in existing defects and the total hydrogen concentration, as suggested from Sofronis and McMeeking (1989) [26], can be written in the form

$$C = C_L + C_T \tag{1.3}$$

It is important to state at this point, that according to McNabb and Foster (1963) [17], the concentrations of hydrogen in these two states are related to each other through the following rate-dependent equation

$$\dot{C}_T = kN_T(1-\theta_T)C_L - \lambda C_T \equiv F(C_L, C_T, \bar{\varepsilon}^p) \tag{1.4}$$

The constant magnitudes though, do not have the same dimensions, since k [=] $\frac{\text{m}^3}{\text{sites}}$ and λ [=] $\frac{1}{\text{s}}$. In order to resolve this issue, k is expressed as $k = \frac{\kappa}{N_L}$ in order to include the variable κ [=] $\frac{1}{\text{s}}$ and eventually,

$$\dot{C}_T = \lambda N_T \left[K_T \theta_L (1-\theta_T) - \theta_T\right] \tag{1.5}$$

Later on, Oriani's theory simplified McNabb's equation by stating that under equilibrium conditions, the population of hydrogen in these two states is such, that the occupancy of the interstitial sites θ_L and the trapping sites θ_T must be consistent with [11]

$$\frac{\theta_T}{1-\theta_T} = \left(\frac{\theta_L}{1-\theta_L}\right) K_T$$

where K_T is defined as

$$K_T = \exp\left(\frac{W_b}{RT}\right)$$

K_T is the equilibrium constant, W_b is the trap binding energy, $R = 8.314\,\frac{\text{J}}{\text{mol}\cdot\text{K}}$ is the universal gas constant, and T is the absolute temperature. In this work the fully transient trapping/de-trapping kinetics theory is used, as dictate by equations (1.4) or (1.5)

1.1.2 Mass balance and diffusion equation

Transport of hydrogen between lattice and trapping sites takes place due to diffusion. The corresponding governing equation is derived using the mass conservation principle. In

particular, let Ω be an arbitrary part of the body under consideration bounded by a surface $\partial\Omega$, at which external loads are applied. The concentration of hydrogen in the NILS C_L, or the trapping sites C_T, that are found within the chosen volume might change over time. This alternation causes mass of hydrogen to flow through the boundary surface. The condition of mass conservation must be met and the respective equation is used, because the change of the total hydrogen concentration C, inside the chosen volume has to be equal with the hydrogen flux through the boundary surface

$$\int_{\Omega} \dot{C}_L \, dV + \int_{\Omega} \dot{C}_T \, dV = \int_{\partial\Omega} J_n \, dS \tag{1.6}$$

Where $J_n = -\mathbf{J} \cdot \mathbf{n}$, with $\mathbf{J}$ being the hydrogen flux, $\mathbf{J}$ [=] H atoms $\cdot \frac{1}{\mathrm{m}^2 \cdot \mathrm{s}}$ and $\mathbf{n}$ is the unit vector that is normal to any point of the boundary surface, facing outwards. After applying the divergence theorem in relation (1.6), the final equation is:

$$\int_{\Omega} \left(\dot{C}_L + \dot{C}_T + \nabla \cdot \mathbf{J} \right) dV = 0 \quad \forall \, \Omega \quad \Rightarrow \quad \dot{C}_L = -\nabla \cdot \mathbf{J} - \dot{C}_T \tag{1.7}$$

The partial differential equation (1.7) is supplemented by the following boundary conditions:

$$C_L(x) = \hat{C}_L(x) = \text{known} \quad \text{on} \quad \partial\Omega_{C_L} \tag{1.8}$$

$$J_n \equiv -\mathbf{J} \cdot \mathbf{n} = \hat{J}_n(x) = \text{known} \quad \text{on} \quad \partial\Omega_{J_n} \tag{1.9}$$

where $\partial\Omega_{C_L} \cup \partial\Omega_{J_n} = \partial\Omega$ and $\partial\Omega_{C_L} \cap \partial\Omega_{J_n} = \emptyset$. Hydrogen flux is assumed to be driven by chemical concentration gradients:

$$\mathbf{J} = -\frac{D_L C_L}{RT} \nabla \mu \tag{1.10}$$

where the chemical potential μ is expressed as

$$\mu(p, C_L) = \mu_0 + RT \ln \left(\frac{C_L}{C_{L0}} \right) - (p - p_0) \bar{V}_H \tag{1.11}$$

with $R = 8.314 \, \frac{\mathrm{J}}{\mathrm{mol} \cdot \mathrm{K}}$ being the gas constant, T the absolute temperature in Kelvin, $\bar{V}_H$ the partial molar volume of hydrogen (in m^3/mol)and $p = \sigma_{kk}/3$ the hydrostatic stress. The quantities C_{L0}, p_0 denote a reference concentration of hydrogen in the lattice and a reference pressure respectively, and μ_0 is the chemical potential corresponding to $C_L = C_{L0}$ and $p = p_0$. Substitution of (1.11) in (1.10), yields

$$\mathbf{J} = -D_L \left(\nabla C_L - \frac{\bar{V}_H}{RT} C_L \nabla p \right) \tag{1.12}$$

where D_L is the lattice diffusion constant and ∇p is the pressure gradient. The equation (1.12) shows that apart from the lattice concentration, the hydrogen flux has a coupled

influence from the mechanical loads, through the pressure gradient, ∇p.

1.2 Mechanical constitutive equations

Before analysing the equations that characterise the elastopalstic behaviour of the material, it must be stated that in this work, one way coupling is being considered and thus, the mechanical behaviour is not influenced from the existence of hydrogen. The coupled equations of the initial-boundary problem of hydrogen diffusion and the elastoplastic boundary value problem are examined. In order to interpret the way hydrogen affects the material's mechanical fields, an adaptation of the von Mises yield criterion is required and will be presented.

Taking into consideration that $\Phi(\boldsymbol{s}, \bar{\varepsilon}^p)$ is the yield function, the yield condition is

$$\Phi(\boldsymbol{s}, \bar{\varepsilon}^p) = 0$$

The total rate of deformation tensor $\mathbf{D}$ is additively decomposed into an elastic part $\mathbf{D}^e$ and a plastic part $\mathbf{D}^p$ [14].

$$\mathbf{D} = \mathbf{D}^e + \mathbf{D}^p \tag{1.13}$$

The corresponding constitutive equations for the elastic and plastic parts are discussed in the following chapters.

1.2.1 Elasticity

Linear, isotropic, hypo-elasticity is assumed so that following the equation (1.13), the elastic rate of deformation tensor $\mathbf{D}^e$ is given as $\mathbf{D}^e = \boldsymbol{\mathcal{M}}^e : \overset{\nabla}{\boldsymbol{\sigma}}$. The Jaumann derivative of the stress tensor is

$$\overset{\nabla}{\boldsymbol{\sigma}} = \dot{\boldsymbol{\sigma}} + \boldsymbol{\sigma} \cdot \mathbf{W} - \mathbf{W} \cdot \boldsymbol{\sigma}$$

with $\mathbf{W}$, spin tensor, being the antisymmetric part of $\boldsymbol{\mathcal{L}}^e$. Also,

$$\boldsymbol{\mathcal{M}}^e = \frac{1}{2G}\,\boldsymbol{\mathcal{K}} + \frac{1}{3\kappa}\,\boldsymbol{\mathcal{J}}$$

and since $\boldsymbol{\mathcal{L}}^e = (\boldsymbol{\mathcal{M}}^e)^{-1}$,

$$\boldsymbol{\mathcal{L}}^e = 2G\boldsymbol{\mathcal{K}} + 3\kappa\boldsymbol{\mathcal{J}}$$

where $\boldsymbol{\mathcal{M}}^e$ is the Elastic compliance tensor and $\boldsymbol{\mathcal{L}}^e$ is the elastic stiffness tensor and G, κ are the elastic shear and bulk modulus of the material.

Considering $\boldsymbol{\mathcal{I}}$ being the symmetric fourth – order identity tensor, then

$$I_{ijkl} = \frac{1}{2}\left(\delta_{ik}\delta_{jl} + \delta_{il}\delta_{jk}\right)$$

$$J_{ijkl} = \frac{1}{3}\left(\delta_{ij}\delta_{kl}\right)$$

and

$$K_{ijkl} = I_{ijkl} - J_{ijkl}$$

1.2.2 Plasticity

The material is assumed to obey the von Mises yield criterion which is written as:

$$\Phi\left(\boldsymbol{s}, \bar{\varepsilon}^p\right) = \sigma_e(\boldsymbol{s}) - \sigma_y(\bar{\varepsilon}^p) = 0 \tag{1.14}$$

where the equivalent stress σ_e, is a function of the deviatoric part of the stress tensor,

$$\sigma_e(\boldsymbol{s}) = \sqrt{\frac{3}{2}\,\boldsymbol{s} : \boldsymbol{s}} \tag{1.15}$$

Also, the yield stress, σ_y, is a function of the equivalent plastic strain. When $\Phi(\boldsymbol{s}, \bar{\varepsilon}^p) > 0$ and no plasticity has still occurred in general, the material acts elastically and $\sigma_y = \sigma_0$ which is the material's initial yield strength. Even so, if the material enters its plastic region, due to hardening, the yield strength will be increased and eventually $\sigma_y\left(\bar{\varepsilon}^p\right) > \sigma_0$, until the hardening rate is zero, $\frac{d\boldsymbol{\sigma}}{d\boldsymbol{\varepsilon}} = 0$, when the point of failure is reached. Thus, the second term of the von Mises yield criterion is the flow stress and is estimated from the power law hardening as

$$\sigma_y\left(\bar{\varepsilon}^p\right) = \sigma_0\left(1 + \frac{\bar{\varepsilon}^p}{\varepsilon_0}\right)^n \tag{1.16}$$

ε_0 is the initial yield strain in the absence of hydrogen and n is the hardening exponent. At the present work, the existence of hydrogen diffusion is neglected due to the one way coupling hypothesis and thus the von Mises yield criterion is expressed as seen in equation (1.14) - (1.16).

Now, if the problem was such, that the mechanical fields would be affected from the hydrogen diffusion, the von Mises yield criterion would have to be modified accordingly, as suggested for instance by Sofronis et al. (2001) [14]

$$\Sigma_y\left(\bar{\varepsilon}^p, C\right) = F(C)\,\sigma_y\left(\bar{\varepsilon}^p\right) \tag{1.17}$$

where F is a suitably chosen degradation function and its accurate form is beyond the scope of the present work.

The stress tensor, $\boldsymbol{\sigma}$, is symmetrical and can be expressed as the summary of a spherical and a deviatoric part, $\boldsymbol{\sigma}^{\mathrm{sph}}$ and $\boldsymbol{\sigma}^{\mathrm{d}}$ or $\boldsymbol{s}$ respectively.

$$\boldsymbol{\sigma} = \boldsymbol{s} + \boldsymbol{\sigma}^{\mathrm{sph}} \tag{1.18}$$

where

$$\boldsymbol{\sigma}^{\text{sph}} = \frac{1}{3}\sigma_{\kappa\kappa}\,\boldsymbol{\delta} \tag{1.19}$$

In order to estimate the plastic part of the total deformation's rate in equation (1.13), due to the Maximum Plastic Work Principle, the normality rule occurs [15] and $\mathbf{D}^p$ is normal at any point belonging to the yield surface. The direction of $\mathbf{D}^p$ can be expressed as

$$\frac{\partial \Phi}{\partial \sigma_{ij}} = N_{ij} = \frac{3}{2\sigma_e} s_{ij} \tag{1.20}$$

and the second order tensor $\mathbf{N}$ has a constant magnitude

$$\mathbf{N} : \mathbf{N} = \frac{3}{2}$$

meaning that the tensor $\mathbf{N}$ expresses only the direction of $\mathbf{D}^p$. Having that in mind, a scalar quantity is considered, $\dot{\lambda}$, to assist fully express $\mathbf{D}^p$ by containing the information about its magnitude in general. Eventually,

$$\mathbf{D}^p = \dot{\lambda}\mathbf{N}$$

Specifically, when working with the von Mises yield criterion,

$$\dot{\bar{\varepsilon}}^p = \sqrt{\frac{2}{3} D^p_{ij} D^p_{ij}}$$

and since $\mathbf{D}^p = \dot{\lambda}\mathbf{N}$,

$$\dot{\bar{\varepsilon}}^p = \dot{\lambda}$$

This way it can be proved that in this specific case,

$$\mathbf{D}^p = \dot{\bar{\varepsilon}}^p \mathbf{N} \tag{1.21}$$

1.2.3 Numerical integration of the constitutive equations

Implementation of the model in a finite element setting (e.g., in ABAQUS) requires the numerical integration of the constitutive equations that were previously presented. Knowing the values of the variables at the beginning of the increment, at time t_n, the values of the same variables must be estimated at the end of the increment, at time t_{n+1}, which is the beginning of the next time step. More specifically, given the values of the following variables

$$F_n,\ \boldsymbol{\sigma}_n,\ \bar{\varepsilon}^p_n,\ C_T\big|_n,\ T_n\ (= C_L\big|_n),\ \text{and}\ F_{n+1},\ T_{n+1}\ (= C_L\big|_{n+1})$$

the values of

$$\boldsymbol{\sigma}_{n+1},\quad \bar{\varepsilon}^p_{n+1},\quad C_T\Big|_{n+1}$$

must be estimated at the end of every increment. Note that T_n $(= C_L|_n)$ and T_{n+1} $(= C_L|_{n+1})$ are applicable equalities due to the mass - heat transfer analogy that will be analysed in Section 2.2.1.

The first step is to integrate the plastic flow rule (1.21), in order to estimate $\Delta\boldsymbol{\varepsilon}^p$, using a backward Euler scheme,

$$\Delta\boldsymbol{\varepsilon}^p = \Delta\bar{\varepsilon}^p\,\mathbf{N}_{n+1} \tag{1.22}$$

In order to find $\Delta\boldsymbol{\varepsilon}^p$, $\Delta\bar{\varepsilon}^p$ must firstly be determined. To achieve that, the following procedure must be followed. Firstly, the equation that estimates $\mathbf{s}_{n+1}$, is

$$\mathbf{s}_{n+1} = \mathbf{s}_n + 2G\,\Delta\boldsymbol{\varepsilon}^e = \mathbf{s}_n + 2G\,(\Delta\boldsymbol{\varepsilon} - \Delta\boldsymbol{\varepsilon}^p) = \underbrace{\mathbf{s}_n + 2G\,\Delta\boldsymbol{\varepsilon}}_{\mathbf{s}^e} - 2G\,\Delta\bar{\varepsilon}^p\,\mathbf{N}_{n+1} \tag{1.23}$$

where $\mathbf{s}^e$ is the known deviatoric elastic predictor.

In view of equation (1.23), it can be shown that $\mathbf{s}_{n+1}$ is co-linear with $\mathbf{s}^e$ as the following equation holds.

$$\mathbf{s}_{n+1} = \frac{1}{1 + \dfrac{3G\,\Delta\bar{\varepsilon}^p}{\sigma_e|_{n+1}}}\,\mathbf{s}^e \tag{1.24}$$

Due to the relation $\mathbf{s}_{n+1}$ and $\mathbf{s}^e$ have in (1.24), by replacing them in (1.20), it eventually leads to

$$\mathbf{N}_{n+1} = \frac{3}{2\,\sigma_e|_{n+1}}\,\mathbf{s}_{n+1} = \frac{3}{2\sigma_e^e}\,\mathbf{s}^e \equiv \mathbf{N}^e = \text{known} \tag{1.25}$$

Now, $\Delta\bar{\varepsilon}^p$ can be estimated by taking the dot product of (1.24) with $\mathbf{N}_{n+1} = \mathbf{N}^e$ and solving for $\sigma_e|_{n+1}$,

$$\underbrace{(\mathbf{s}_{n+1} : \mathbf{N}_{n+1})}_{\sigma_e|_{n+1}} = \underbrace{(\mathbf{s}^e : \mathbf{N}^e)}_{\sigma_e^e} - 2G\Delta\bar{\varepsilon}^p\,\underbrace{(\mathbf{N}_{n+1} : \mathbf{N}_{n+1})}_{\frac{3}{2}} \quad \Rightarrow \quad \sigma_e|_{n+1} = \sigma_e^e - 3G\Delta\bar{\varepsilon}^p. \tag{1.26}$$

where σ_e^e is the von Mises elastic stress, associated with the elastic predictor $\mathbf{s}^e$. Knowing the σ_e^e from (1.26), the von Mises yield criterion is

$$\Phi(\mathbf{s}_{n+1}, \Delta\bar{\varepsilon}^p) \equiv \sigma_e^e - 3G\Delta\bar{\varepsilon}^p - \sigma_y\,(\bar{\varepsilon}_n^p + \Delta\bar{\varepsilon}^p) = 0 \tag{1.27}$$

Equation (1.27) is a non-linear equation which can be solved numerically for $\Delta\bar{\varepsilon}^p$ using the numerical Newton's method. In this case, a reasonable first estimate for $\Delta\bar{\varepsilon}^p$ can be found by approximating (1.27) as

$$\sigma_e^e - 3G\,\Delta\bar{\varepsilon}^p - \left[\sigma_y(\bar{\varepsilon}_n^p) + \left.\frac{\partial\sigma_y}{\partial\bar{\varepsilon}^p}\right|_{\bar{\varepsilon}^p=\bar{\varepsilon}_n^p}\Delta\bar{\varepsilon}^p\right] = 0$$

$$\Rightarrow \quad \Delta\bar{\varepsilon}^p = \frac{\sigma_e^e - \sigma_y(\bar{\varepsilon}_n^p)}{3G + \frac{\partial\sigma_y(\bar{\varepsilon}^p)}{\partial\bar{\varepsilon}^p}\Big|_{\bar{\varepsilon}^p=\bar{\varepsilon}_n^p}} \tag{1.28}$$

After $\Delta\bar{\varepsilon}^p$ has been determined, $\mathbf{s}_{n+1}$ can be calculated using (1.24)

$$\mathbf{s}_{n+1} = \mathbf{s}^e - 2G\,\Delta\bar{\varepsilon}^p\,\mathbf{N}_{n+1} = \text{known} \tag{1.29}$$

Using (1.29), $\boldsymbol{\sigma}_{n+1}$ can be now calculated as

$$\boldsymbol{\sigma}_{n+1} = \boldsymbol{s}_{n+1} + p_{n+1}\,\boldsymbol{\delta} \tag{1.30}$$

In order to estimate $\boldsymbol{\sigma}_{n+1}$, the value of p_{n+1} must also be found. To achieve that, notice

$$p_{n+1} = \kappa\,\varepsilon^e_{kk}|_{n+1} = \kappa\,\varepsilon_{kk}|_{n+1}$$

or

$$p_{n+1} = p_n + \kappa\,\Delta\varepsilon^e_{kk} = \underbrace{p_n + \kappa\,\Delta\varepsilon_{kk}}_{p^e} = p^e$$

After finding $\bar{\varepsilon}^p_{n+1}$ from $\Delta\bar{\varepsilon}^p = \bar{\varepsilon}^p_{n+1} - \bar{\varepsilon}^p_n$, using (1.28) and $\boldsymbol{\sigma}_{n+1}$ from (1.30), the last variable that must be estimated, is $C_T\big|_{n+1}$. By integrating (1.5), using a backward Euler scheme like at the beginning of the procedure,

$$\frac{C_T\big|_{n+1} - C_T\big|_n}{\Delta t} = \lambda\left[K_T\,\theta_L\big|_{n+1}\left(N_T\big|_{n+1} - C_T\big|_{n+1}\right) - C_T\big|_{n+1}\right]$$

$$\Rightarrow \quad C_T\big|_{n+1} = \frac{C_T\big|_n + K_T\,\theta_L\big|_{n+1}\,N_T\big|_{n+1}\lambda\Delta t}{1 + (1 + K_T\,\theta_L\big|_{n+1})\lambda\Delta t}, \quad \theta_L|_{n+1} = \frac{C_L|_{n+1}}{N_L} \tag{1.31}$$

and the integration process is completed.

1.3 Linear elastic fracture mechanics

The goal of this work, is to eventually estimate the hydrogen concentration and mechanical fields at the tip of an axial crack. It is considered that uniform pressure is applied at the surfaces of the crack and the problem is analysed under Mode-I and plane strain conditions. Thus, the theory of Fracture Mechanics is used, in order to estimate the analytical solutions of the stress fields [18], σ_{11} and σ_{22}, along with the asymptotic displacements of William's (2007) singular linear elastic field [19] that are imposed on the outer boundary of the domain. Also, both the K_I and T-stress terms should be employed to characterize how the stress and deformation fields influence each other, since the near-tip solutions cannot be accurately predicted using a standard boundary layer approach that neglects the T-stress,

as suggested by Dadfarnia et al. (2008) [8].

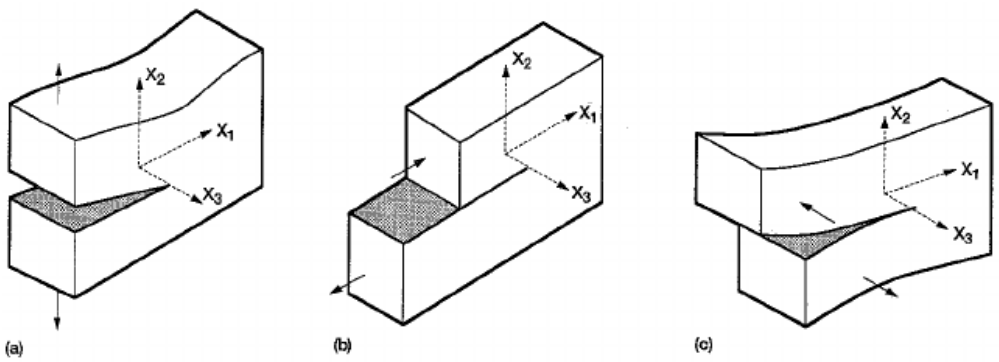

Figure 1.2: Modes of loading in fracture mechanics [22]. (a) Mode-I (b) Mode-II (c) Mode-III

Mode-I loading describes the scenario where due to stresses acting normal to the crack surfaces, the crack propagates perpendicularly to its plane of symmetry, along X_1 axis and is depicted in Fig.1.2. Failure occurs when the stress intensity factor, K_I, which quantifies the intensity of the stress field near the tip of the crack, reaches the value of the material's fracture toughness, K_{IC}. In what follows, a brief outline of the Mode-I asymptotic solution is given.

In order to fully describe the plane-strain problem, a stress function must be formulated, in order satisfy the corresponding biharmonic equation, (1.32). This function is called Airy stress function, f

$$\nabla^4 f = 0 \tag{1.32}$$

The asymptotic solution of this function, in order to examine the mechanical fields near the crack tip, where theoretically the stresses tend to be infinite due to $r \to 0$ being a singular point, is

$$f(r,\theta) = \sum_{i=1}^{\infty} r^{\lambda_i+1} F_i(\theta,\lambda_i) \tag{1.33}$$

Where θ is the angular coordinate of the point at which the Airy function is being evaluated, as it is shown in Fig.1.3, r is the distance from the crack tip, λ_i are the eigenvalues of the problem, and $F_i(\theta,\lambda_i)$ are the corresponding angular eigenfunctions.

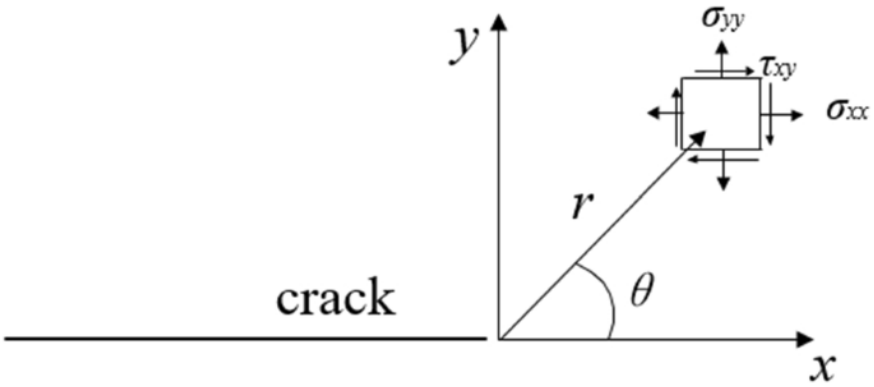

Figure 1.3: The coordinates needed for the Airy function [23].

If the crack face is traction free, the boundary conditions for the first and second terms in the asymptotic solution are

$$\sigma_{\theta\theta}(r, \theta = \pm\pi) = 0, \quad \sigma_{r\theta}(r, \theta = \pm\pi) = 0$$

and solving for the first two eigenvalues, λ_1 and λ_2, which respectively have the values of $1/2$ and 1, the first two terms are estimated and the stress field along with the displacements can be estimated.

$$\mathbf{u}(r,\theta) = \begin{bmatrix} u_x(r,\theta) \\ u_y(r,\theta) \end{bmatrix} = K_I \left(\frac{1+\nu}{E}\right) \sqrt{\frac{r}{2\pi}} \begin{bmatrix} \cos\left(\frac{\theta}{2}\right)(3-4\nu-\cos\theta) \\ \sin\left(\frac{\theta}{2}\right)(3-4\nu-\cos\theta) \end{bmatrix} + T \begin{bmatrix} \left(\frac{1-\nu^2}{E}\right) r\cos\theta \\ -\left(\frac{\nu(1+\nu)}{E}\right) r\sin\theta \end{bmatrix}$$

$$\boldsymbol{\sigma}(r,\theta) = \begin{bmatrix} \sigma_{11}(r,\theta) \\ \sigma_{22}(r,\theta) \end{bmatrix} = \frac{K_I}{\sqrt{2\pi r}} \frac{1}{4} \begin{bmatrix} 3\cos\left(\frac{\theta}{2}\right) + \cos\left(\frac{5\theta}{2}\right) \\ 5\cos\left(\frac{\theta}{2}\right) - \cos\left(\frac{5\theta}{2}\right) \end{bmatrix} + \begin{bmatrix} T \\ 0 \end{bmatrix}$$

If there is a homogeneous pressure applied at the crack face, as it is considered in the present work, the boundary conditions for the second term are modified as

$$\sigma_{\theta\theta}(r, \theta = \pm\pi) = -p, \quad \sigma_{r\theta}(r, \theta = \pm\pi) = 0$$

and the first two terms of the asymptotic solution take the form

$$\begin{aligned} u_x(r,\theta) = K_I \left(\frac{1+\nu}{E}\right) \sqrt{\frac{r}{2\pi}} \cos\left(\frac{\theta}{2}\right) [3-4\nu-\cos(\theta)] \\ + T\left(\frac{1-\nu^2}{E}\right) r\cos(\theta) - \frac{p(1-2\nu)}{2G} r\cos(\theta) \end{aligned} \tag{1.34}$$

$$u_y(r,\theta) = K_I \left(\frac{1+\nu}{E}\right)\sqrt{\frac{r}{2\pi}}\sin\left(\frac{\theta}{2}\right)\left[3-4\nu-\cos(\theta)\right] - T\left(\frac{\nu(1+\nu)}{E}\right) r\sin(\theta) - \frac{p(1-2\nu)}{2G} r\sin(\theta) \tag{1.35}$$

The corresponding solution for the stress fields is

$$\sigma_{11}(r,\theta) = \underbrace{\frac{K_I}{\sqrt{2\pi r}}\frac{1}{4}\left[3\cos\left(\frac{\theta}{2}\right)+\cos\left(\frac{5\theta}{2}\right)\right]}_{\text{First term}} + \underbrace{T-p}_{\text{Second term}} \tag{1.36}$$

$$\sigma_{22}(r,\theta) = \underbrace{\frac{K_I}{\sqrt{2\pi r}}\frac{1}{4}\left[5\cos\left(\frac{\theta}{2}\right)-\cos\left(\frac{5\theta}{2}\right)\right]}_{\text{First term}} - \underbrace{p}_{\text{Second term}} \tag{1.37}$$

In the numerical simulations that follow, the asymptotic displacement fields, being characterised by both the stress intensity factor K_I and the T-stress, will be used as boundary conditions for the modified layer formulation. The asymptotic stress fields (1.36) - (1.37) will be used to assess the accuracy of the corresponding numerical results.

Chapter 2

FEA Model, Results and Comparisson

Having described the fundamental theoretical background, this chapter deals with the details of the simulation set-up and the description of the numerical results. In particular, in this chapter, the boundary and initial conditions are shown , the analogy between heat and mass transfer is explained, and the material properties are given.

Eventually, since the models for the SENT specimen, [24], and the Small Scale Yielding (SSY) approach were complete, in order to check if their results they numerically agree and visualize the results, a comparison was made. The distributions of both mechanical and hydrogen fields ahead of the crack tip and in the whole domain of the solution are shown and discussed.

All the numerical results were extracted from the ABAQUS FEA software, and then imported to a MATLAB file in order to generate the necessary plots.

2.1 The problem in question

Initially, the real problem taken into consideration refers to gaseous hydrogen flowing at pressure of 15 MPa through a pipe made of medium or low strength steel and a yield strength less than 750 MPa. The loading conditions are considered to be Mode-I in plane strain, since the specimen used for the analysis has an axial crack formed on its inner diameter.

It has been proven, that the mechanical fields developing near the tip of a pipeline's axial crack can be estimated by using a Single Edge Notch Tension (SENT) specimen [7]. Then, in order to view the problem closer to the region of interest, the crack tip, a modified boundary layer formulation is used under the small scale yielding (SSY) hypothesis. The present work approaches the SSY formulation and in order to evaluate the reliability of the simulation, the results are compared with the SENT specimen analysis, [24], and a research that was conducted in the past from Dadfarnia et al. (2011) [7], referring to a SENT specimen as well.

The initial and boundary conditions used, are shown in Fig. 2.1. In order to fully describe the mechanical fields, both K_I and T-stress parameters are used.In the simulation models, the initial condition that is used, is that the NILS hydrogen concentration, is $C_L(t = 0) = 0$,

thus considering the domain initially hydrogen free, since as initially $\bar{\varepsilon}^p = 0$, $C_T = 0$ as well, as shown in Fig.1.1. Two boundary conditions are used as well. Firstly, $C_L(p)$ at the surfaces of the examined area that come in contact with the flowing hydrogen, meaning that it is always in equilibrium with the hydrogen in the pipe, as explained by Sieverts law [20]. Secondly, due to symmetry, half the pipeline is examined and the plane of symmetry is assigned with no flux and so, no hydrogen atoms pass through that surface.

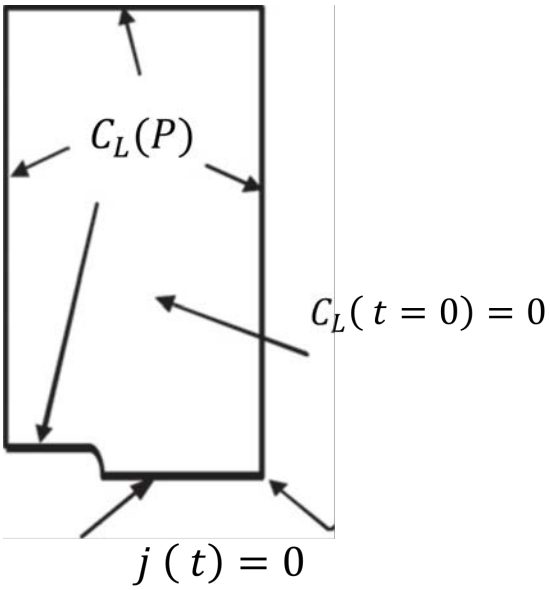

(a)

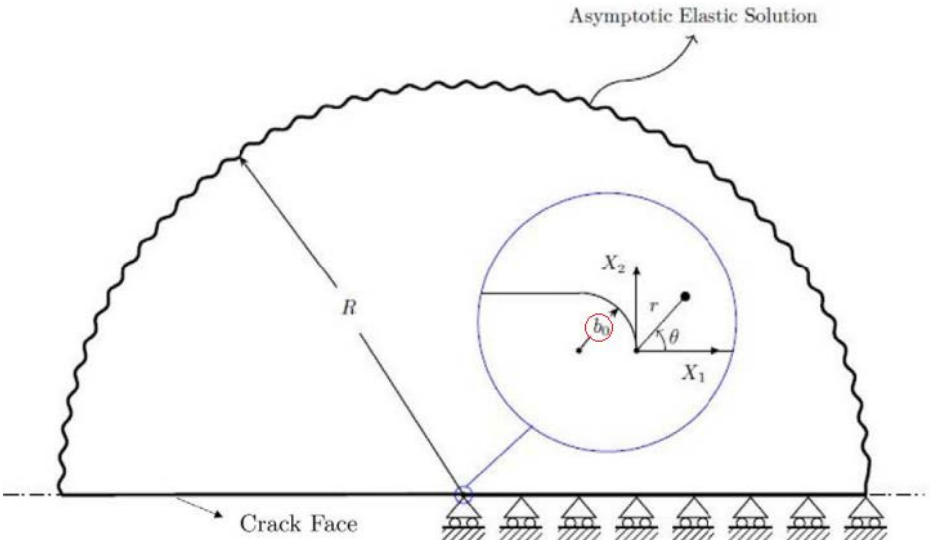

(b)

Figure 2.1: The initial and boundary conditions of the SENT specimen and boundary layer formulation respectively.

The mechanical load, $p = 15\,\text{MPa}$, is applied on the crack surface and the asymptotic displacement field was applied on the outer surface. Its magnitude rises linearly from 0 MPa to 15 MPa in 1 second and remains constant for the remaining duration of the simulation, until steady state. The hydrogen diffusion is imposed on the crack surface and linearly as

well. At 0 second, due to the initial condition, $C_L = 0$, but after 1 second, $C_L = 2.659 \cdot 10^{22}$ H atoms/m^3 because of the Sieverts law for $p = 15$ MPa.

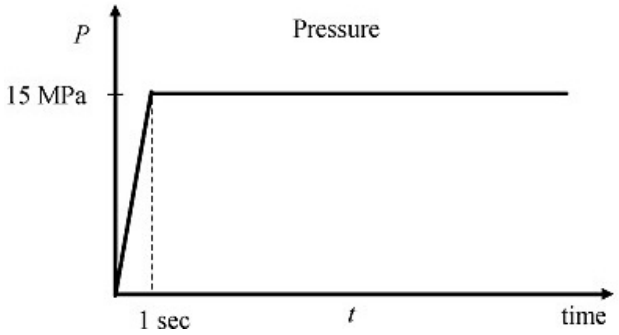

Figure 2.2: The applied pressure at the crack face as a function of time [8].

2.2 The finite element model

2.2.1 Heat transfer - Mass diffusion analogy

Due to lack of flexibility ABAQUS has in simulating a coupled stress - mass transfer analysis without developing user-defined finite elements, an analogy between the diffusion and heat transfer problem is utilised, which is an approach broadly used [25]. This approach allows to take advantage of the built in capabilities of ABAQUS in solving coupled mechanical-heat transfer problems under appropriate variable identifications. Hence, a coupled stress-heat transfer problem is formed, where the temperature represents the NILS concentration, C_L, in order to numerically approach the real problem as sufficient as possible.

In order to apply the analogy in the simulations, a couple of custom user-subroutines had to be utilized, such as UMAT and UMATH. Also, the *COUPLED TEMPERATURE-DISPLACEMENT option was used in ABAQUS/Standard, instead of the *STATIC that would be utilized if the problem was solely mechanical.

As hypothesized in subsection 1.1.2, when the mass balance of the diffusing hydrogen atoms was analysed, an arbitrary part of the material is considered, with volume Ω and $\partial\Omega$ being the boundary surface. Also, $\mathbf{n}$ is a unit vector, normal to any point of the boundary surface, $\partial\Omega$, facing outwards.

Now, the energy balance equation can be described as

$$\int_{\Omega} \rho \dot{\bar{U}}\, dV = \int_{\partial\Omega} q_n\, dS + \int_{\Omega} r\, dV \quad \forall\, \Omega \tag{2.1}$$

Where ρ [=] kg m^{-3} is the mass density and $\bar{U}$ is the internal energy per unit mass (J kg^{-1}). Also, the thermal energy provided by a heat source in the selected volume, is r [=] W m^{-3} and $\mathbf{q}$ is the heat flux per unit area, with q [=] W m^{-2}. In order to use the Gauss divergence theorem in equation (2.1), $q_n \equiv -\mathbf{q} \cdot \mathbf{n}$ will be used,so as to eventually have only volumetric

integrations. The magnitude of q_n, expresses the thermal energy that enters the chosen, arbitrary volume Ω through its boundary surface $\partial\Omega$. Eventually,

$$\int_{\Omega} \left(\rho\dot{\bar{U}} + \nabla\cdot\mathbf{q} - r\right) dV = 0 \quad \forall\,\Omega \implies \quad \rho\dot{\bar{U}} = -\nabla\cdot\mathbf{q} + r \tag{2.2}$$

but knowing that $\dot{\rho} = -\rho D_{kk}$, where $\mathbf{D}$ is the rate of deformation gradient, the equation (2.2) can be written as

$$\dot{\overline{\rho\bar{U}}} - \dot{\rho}\bar{U} + \nabla\cdot\mathbf{q} = r \Rightarrow \dot{\overline{\rho\bar{U}}} = -\nabla\cdot\mathbf{q} + \left(r - D_{kk}\rho\bar{U}\right) \tag{2.3}$$

For small elastic strains ($D^e_{kk} \approx 0$) and plastically incompressible materials ($D^p_{kk} = 0$), the relation $D_{kk} = D^e_{kk} + D^p_{kk} = 0$ holds and equation (2.3) can be simplified as:

$$\dot{\overline{\rho\bar{U}}} = -\nabla\cdot\mathbf{q} + r \tag{2.4}$$

By comparing the relations that express the heat and mass transfer phenomena, equations (2.2) and (1.7) respectively, it can be concluded that the NILS hydrogen concentration C_L can be estimated through the temperature field T, after solving the coupled temperature - displacement problem.

Table 2.1: Analogy between heat transfer and mass diffusion for a plastically incompressible material.

Heat Transfer		**Mass Diffusion**
Temperature: T	$\leftrightarrow$	Lattice hydrogen concentration: C_L
Internal energy: $\bar{U}(\Delta\boldsymbol{\varepsilon}, T)$	$\leftrightarrow$	$\frac{C_L - C_{L0}}{\rho(\Delta\varepsilon)}$
Heat flux: $\mathbf{q}$	$\leftrightarrow$	Hydrogen flux: $\mathbf{J}$
$\dot{\overline{\rho\bar{U}}} = -\nabla\cdot\mathbf{q} + \left(r - \rho D_{kk}\dot{\bar{U}}\right)$	$\leftrightarrow$	$\dot{C}_L = -\nabla\cdot\mathbf{J} - \dot{C}_T$
$T(\mathbf{x}) = \hat{T}(\mathbf{x}) =$ given on $\partial\Omega_T$	$\leftrightarrow$	$C_L(\mathbf{x}) = \hat{C}_L(\mathbf{x}) =$ given on $\partial\Omega_{C_L}$
$q_n = -\mathbf{q}\cdot\mathbf{n} = \hat{q}(\mathbf{x}) =$ given on $\partial\Omega_q$	$\leftrightarrow$	$J_n = -\mathbf{J}\cdot\mathbf{n} = \hat{J}_n(\mathbf{x}) =$ given on $\partial\Omega_{J_n}$

What can be seen from Table 2.1, is that the lattice hydrogen concentration C_L and the hydrogen flux $\mathbf{J}$, are respectively identified as temperature T and heat flux $\mathbf{q}$. Also, there is an obvious analogy between the mass and energy balance equations and their corresponding boundary conditions as they are presented in Sections 1.1.2 and 2.2.1.

2.2.2 Model Parameters

The boundary layer formulation is a sufficient way to simplify the SENT specimen formulation, since the area under examination is near the crack tip instead of the whole specimen domain. The findings are compared to the results of a 2-D analysis, conducted by Dadfarnia et al.(2011) [7].

Table 2.2: SENT specimen dimensions

Magnitude	**Measurement Unit**
Width: W	10 mm
Height: H	50 mm
Crack length: a	2.08 mm
Initial radius of crack opening: b_0	1 μm

The dimensions of the SENT specimen that were used initially, in order to eventually reach the SSY hypothesis, are given in Table 2.2 and due to symmetry, using H/2, they correspond to Fig.2.1a.

Table 2.3: Material properties for steel pipe.

Magnitude	**Measurement Unit**
Young's Modulus: E	201.88 GPa
Poisson's ratio: ν	0.3
Crack length: a	2.08 mm
Yield stress: σ_0	595 MPa
Work hardening exponent : n	0.059

The properties of the material that is used, are given in Table 2.3.

The dimensions of the specimen are such, so that under specific loading which is beyond this work's subject, but analysed thoroughly from Dadfarnia et al. (2011) [7], the stress intensity factor and the T-stress that are applied on the boundary layer are respectively $K_I = 34.12\,\text{MPa}\sqrt{\text{m}}$ and T-stress $= -188.02$MPa.

After an initial simulation of the SENT specimen was completed, the plastic zone was checked in order to see what dimension would be safe to use for the SSY formulation. Since the maximum radius of the plastic zone at the SENT specimen simulation was found to be 1.732 mm as seen in Fig.2.3a, a semi-circle domain was considered and its boundary surface was loaded by remote displacements, as they are expressed at eqs. (1.34) and (1.35). The radius of the semi - circle, was chosen to be 2 mm, since it would include the formed plastic zone while not exceeding the SENT specimen's dimensions, as the crack length is $a = 2.08$mm. The plastic zone at the boundary layer formulation, was later estimated to be 1.249 mm.

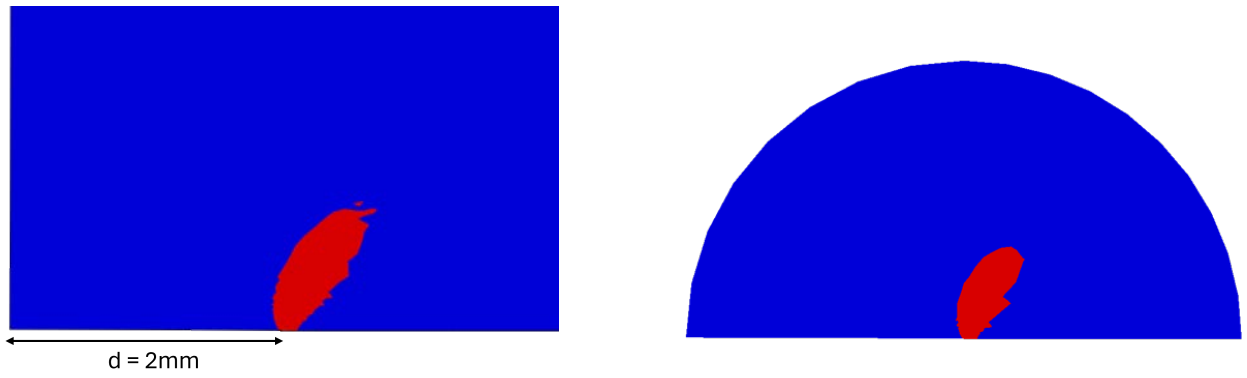

(a) (b)

Figure 2.3: The plastic zone of (a) the SENT specimen [24] and (b) the boundary layer formulation.

Eventually, after properly meshing the domain in order to avoid divergence at the final results due to lack of sufficient integration nodal points, the number of nodes used for this analysis was 1971 and 1856 type CPE4HT elements were composing the final meshed domain.

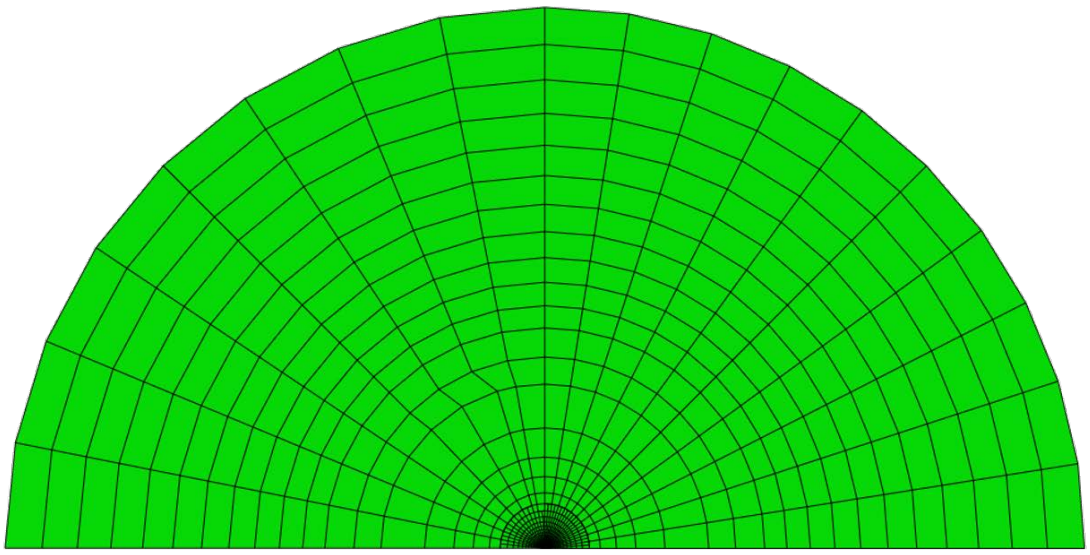

Figure 2.4: Finite element discretization of the boundary layer.

The rate at which the hydrogen diffusion and the pressure are applied linearly at the crack face has been discussed. Apart from that, at the lower surface where no flux is imposed, a boundary condition is also applied, preventing the nodes of the surface to move vertically, due to the existing symmetry.

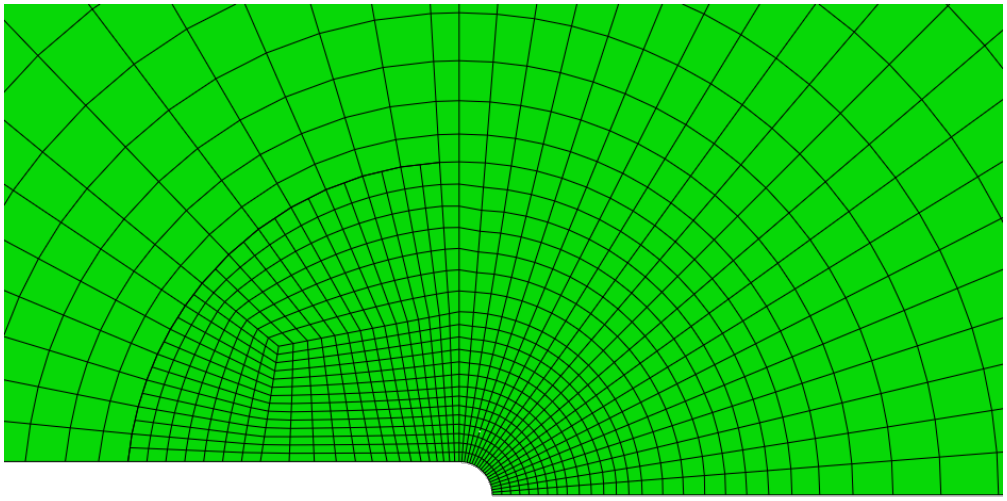

Figure 2.5: Zoomed meshing at a domain where each visible side has a distance of 10 μm from the crack tip.

In order to avoid possible numerical instabilities due to the discrepancy among the magnitudes of the coupled mechanical and diffusion equations, all the magnitudes that were used through the set-up of the analysis were dimensionless.

Table 2.4: Normalizing parameters.

Symbol	Unit	Value
ℓ_0	m	1×10^{-6}
t_0	s	1
C_0	H atoms/m^3	2.659×10^{22}
R	J/(mol·K)	8.314
T	K	300
Σ_0	Pa	595×10^6

Table 2.5: Normalization of relevant quantities.

Normalized Quantity	Expression
$\hat{E}$	E/Σ_0
$\hat{\sigma}_0$	σ_0/Σ_0
$\hat{N}_L$	N_L/C_0
$\hat{D}$	$D/(\ell_0^2/t_0)$
$\hat{V}_H$	$V_H/(RT/\varepsilon_0)$
$\hat{N}_T$	N_T/C_0

How each quantity is being normalized can be seen in Table 2.5, based on the normalizing parameters in Table 2.4.

2.3 Numerical results

2.3.1 Initial evaluation

At this point, it must be stated that the models were initially evaluated under two circumstances. A comparison among the numerical results of the modified boundary layer hypothesis with the SENT specimen simulations and some existing data occurred using only the first term of the displacement boundary layer and using both terms, as seen in Section 1.3. It was observed, that the absence of the second term caused a significant deviation to the results of the boundary layer formulation analysis and thus in all the results presented, both the K_I and T-stress terms were considered.

At first, in order to see if the model was properly set, the mechanical fields were examined. An important observation, was that the hypothesized one way coupling can indeed be observed, since the simulations were examined both with the existence of hydrogen diffusion and with its absence. In the final results, the mechanical fields were identical near the crack tip. Finally, the fields do not alternate after 1 second, from when afterwards the applied pressure remains constant.

The first comparison that was made, was the magnitude of hydrostatic stress, $p = \sigma_{kk}/3$. All the results given refer to steady state $t = 2.75 hours$, unless said otherwise.

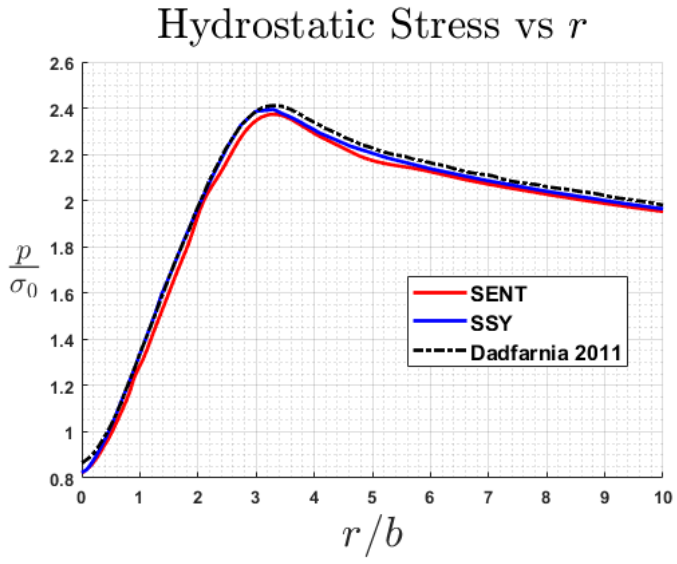

Figure 2.6: The path plot of the hydrostatic stress p/σ_0 ahead of the crack tip.

In Fig.2.6, the red curve represents the numerical results of the normalized hydrostatic stress in the SENT specimen. The blue curve refers to the SSY approach and the dashed black curve corresponds to the results given in [7]. The boundary layer hypothesis agrees with the corresponding numerical results of Dadfarnia et al. (2011) and the peak value is reached at a distance $\frac{r}{b} = 3$ in all cases.

In order to normalize the distance, r, from the crack tip, the final radius of the crack opening b is used, where $b = b_0 + u_2 = 3.2886$ μm. It can be found in Table 2.2, that b_0 is

the initial radius of the crack opening and u_2, being the displacement in X_2 axis due to the resulting stress that is analysed in Section 1.3, estimated at the node vertically above point $O(0,0)$ is $u_2 = 2.2886\ \mu$m.

After observing the plot in Fig. 2.6, there is minimal deviation among the results of interest. The contour plots for $\frac{p}{\sigma_0}$ can be seen in Fig. 2.7.

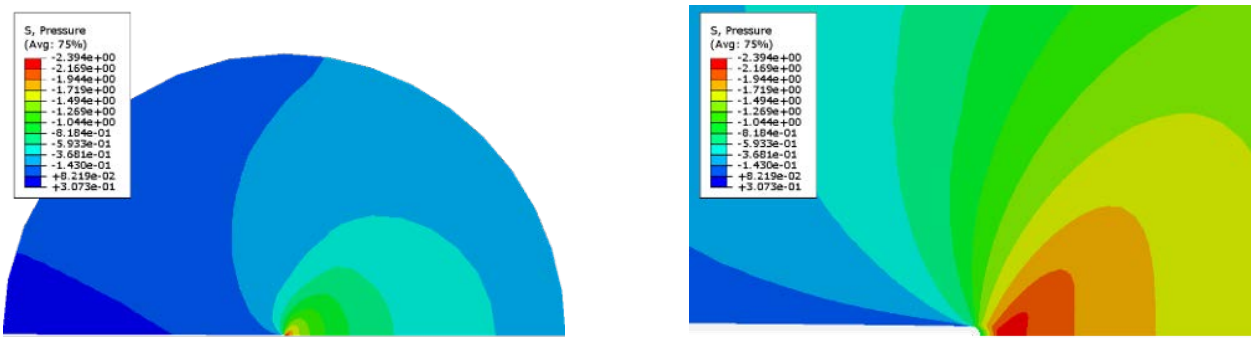

(a) (b)

Figure 2.7: Distribution of the hydrostatic stress p/σ_0 (a) in the whole domain and (b) near the crack tip.

Next, the equivalent plastic strain, $\bar{\varepsilon}^p$, was the objective of the comparison, in order to fully view the model's reliability, regarding the mechanical fields. The curves respectively refer to the SENT specimen, the boundary layer formulation and the work research of Dadfarnia et al. (2011).

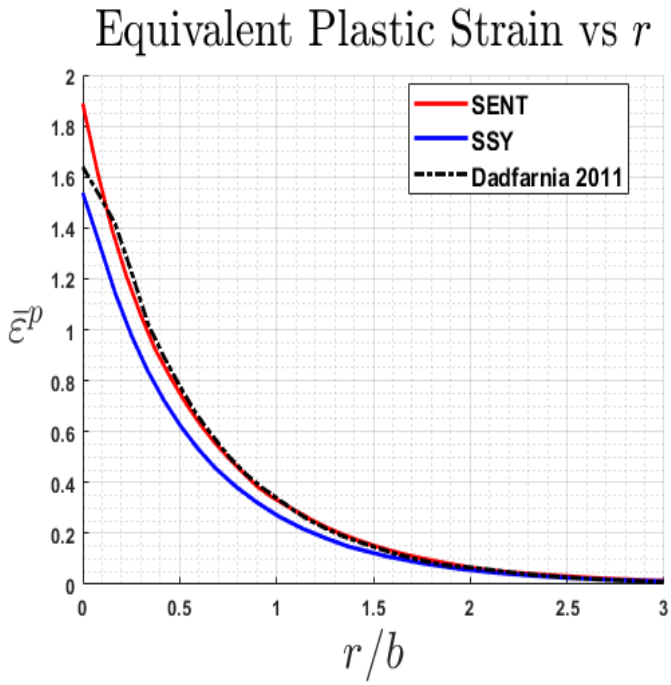

Figure 2.8: The equivalent plastic strain, $\bar{\varepsilon}^p$, near the crack tip.

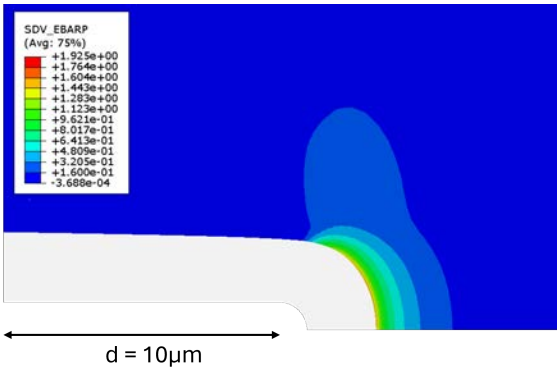

Figure 2.9: The contour plot of the equivalent plastic strain at the crack tip.

It can be seen in Fig. 2.8, that the results agree reasonably well in all cases and only differ slightly as $r \to 0$. Even so, the boundary layer formulation sufficiently describes the strain field which is visualised in Fig. 2.9

2.3.2 Stress fields

In this section, the numerical results of fully elastic and elastoplastic simulations are being compared with the asymptotic solutions. Firstly, the σ_{11} will be depicted. It can be seen from equation (1.36), that the analytical solution for σ_{11} consists out of two terms. In order to find the K_I dominance area and evaluate the convergence of the numerical solutions, the analytical solution,(1.36), was estimated both for one and two terms and they were placed in the same path plot with the numerical solutions.

In Fig 2.10 - 2.13, the σ_{11} and σ_{22} are being depicted along the symmetry plane in front of the crack tip. The green and red curves represent the analytical solutions with one and two terms respectively and the black and dashed blue curves are the numerical results for the elastoplastic and elastic solutions.

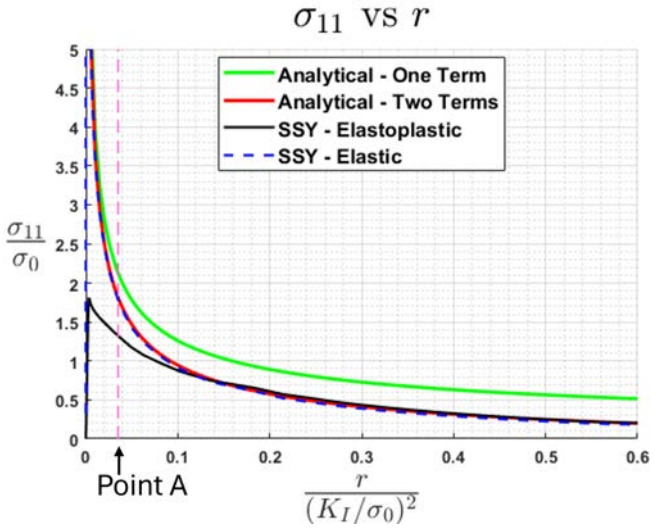

Figure 2.10: Comparisson between the analytical and numerical prediction for σ_{11}/σ_0.

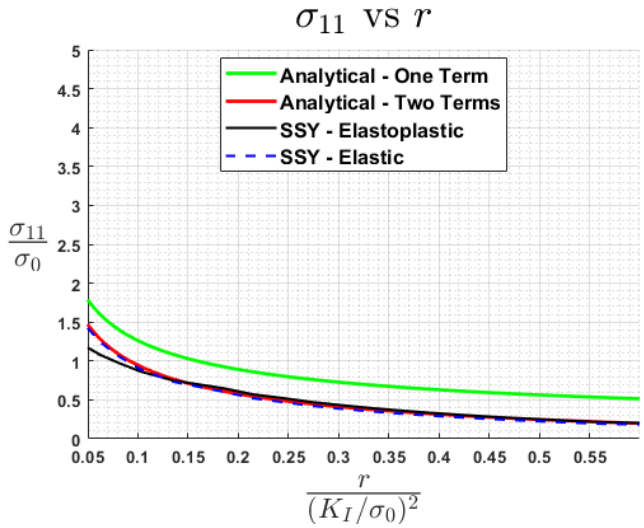

Figure 2.11: Analytical and numerical solutions of σ_{11}/σ_0 in the elastic region.

From Fig. 2.10 and 2.11, a couple of conclusions can be drawn. Firstly, in Fig. 2.10, the K_I dominance area is the length where the analytical solutions do not deviate from one another. Also, the vertical curve represents the point at which the elastic region begins, for $\theta = 0$ and any point of the path after point A has not been plastically deformed. It can be observed in 2.11 that the numerical, elastoplastic solution tends to the analytical solution with both terms included. The reason why the numerical solution is diverged from the analytical ones near the tip, before point A, is the existence of singularity and theoretically the magnitude of the stresses is infinite, but in reality plasticity occurs.

The same procedure was followed with σ_{22}, but it can be seen in equation (1.37) that the T-stress does not enter the analytical solution. Even so, the applied pressure affects the analytical solution and it had to be taken into consideration. It can be seen though in Fig.2.13, that the effect of pressure to the analytical solution is negligible, since the analytical solutions for one and two terms are almost identical.

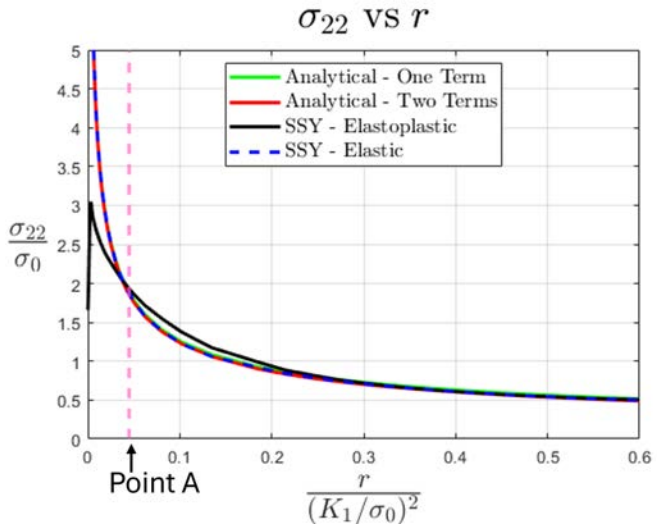

Figure 2.12: Comparisson between the analytical and numerical prediction for σ_{22}/σ_0.

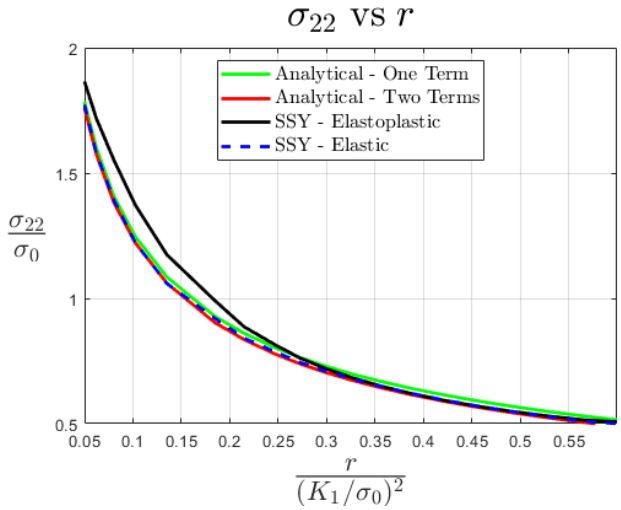

Figure 2.13: Analytical and numerical solutions of σ_{22}/σ_0 in the elastic region.

The results for the elastoplastic solutions were compared with the SENT specimen in steady state. So, near the crack tip, the stress fields σ_{11} and σ_{22} are:

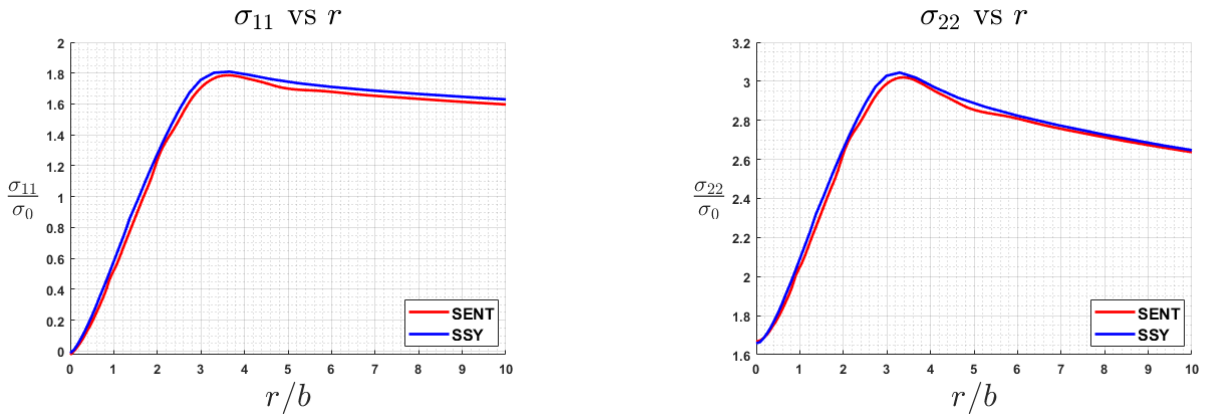

(a) (b)

Figure 2.14: SENT specimen and boundary layer formulation comparison for σ_{11}/σ_0 and σ_{22}/σ_0.

At Fig. 2.14a and 2.14b, the red line depicts the numerical results of the SENT analysis,[24], and the blue curve represents the results of the SSY approach. It is observed that the two curves are quite similar to one another. Also, at Fig. 2.15 the distributed σ_{11} and σ_{22} are respectively depicted in the whole SSY domain.

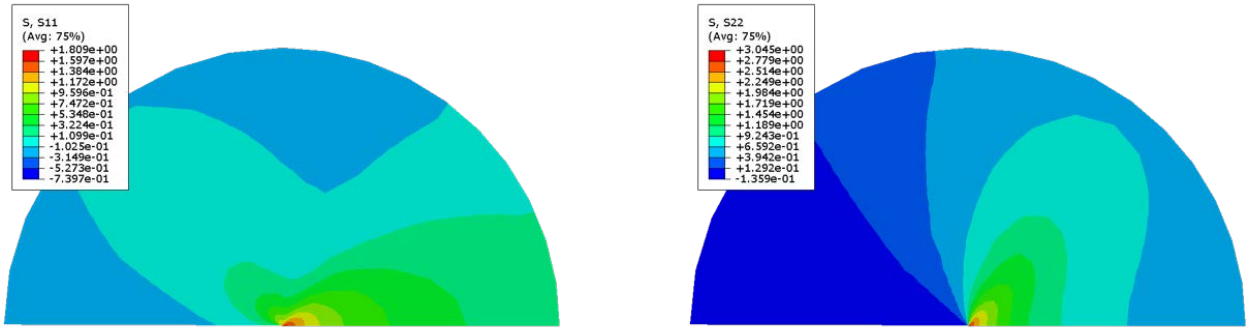

(a) (b)

Figure 2.15: Stress fields' contour plots in the boundary layer formulation for (a) σ_{11} and (b) σ_{22}.

2.3.3 Hydrogen concentration fields

In Section 1.1.1, the theory of hydrogen transport is being showcased. In order to fully define the hydrogen concentration fields, the magnitudes of C_L, C_T and C must be estimated at the same path near the crack tip where the mechanical fields were found in Section 2.3.2.

As before, the red curve represents the SENT specimen results, the blue line refers to the SSY and the dashed black one refers to [7].

Firstly, the hydrogen concentration in NILS and trapping sites, C_L and C_T respectively, were numerically calculated in steady state, by utilizing the ability ABAQUS has in simulating a mass transfer problem as a heat transfer one, as explained in Section 2.2.1. The results of the simulations can be seen in Fig. 2.16. The difference of the scale at both the vertical and horizontal axis should be noticed.

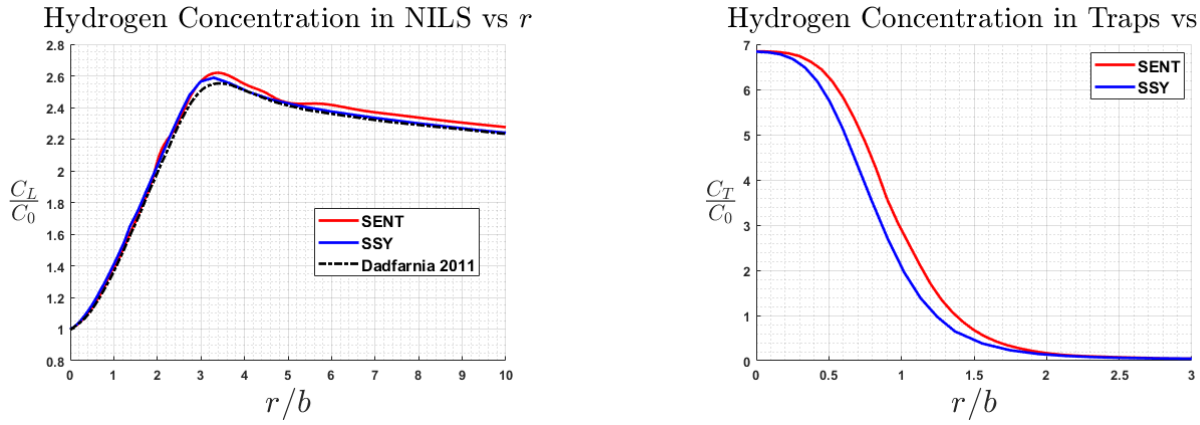

(a) (b)

Figure 2.16: (a) $\frac{C_L}{C_0}$ and (b) $\frac{C_T}{C_0}$ hydrogen concentration path plots ahead of the crack tip.

From Fig. 2.16, a couple of observations can be made. Firstly, C_L reaches its peak value when $\frac{r}{b} = 3$, which is the same dimensionless distance where the hydrostatic stress

reaches its maximum magnitude as well, as seen in Fig. 2.6. Also, the trapped hydrogen concentration takes its maximum value near the crack tip, since from that point afterwards, due to plastic deformation the trapping sites are saturated and hence less hydrogen atoms are being trapped. With that in mind, due to plasticity and a high equivalent plastic strain, near the crack tip the trapping sites are the dominant cause of hydrogen concentration and while moving along the symmetry plane due to traps' saturation and elasticity, migrating through the NILS is the dominant reason of hydrogen concentration.

The discrepancies in the numerical results for C_T shown in Fig. 2.16b can be explained by the relationship between N_T and the equivalent plastic strain discussed in Section 1.1.1, as well as the differing behaviours of the SSY and SENT formulations concerning the equivalent plastic strain illustrated in Fig. 2.8. Since the equivalent plastic strain magnitude at the crack tip surpasses the saturation point of N_T, at both formulations, the value of C_T at the crack tip is the same.

The total hydrogen concentration was also calculated. The three magnitudes of interest were placed in the same graph, in order to visually observe that $C = C_L + C_T$ when steady state has been reached. The moment when C_T reaches its constant value, which is almost zero due to trapping saturation, the dominant term of the total hydrogen concentration is C_L.

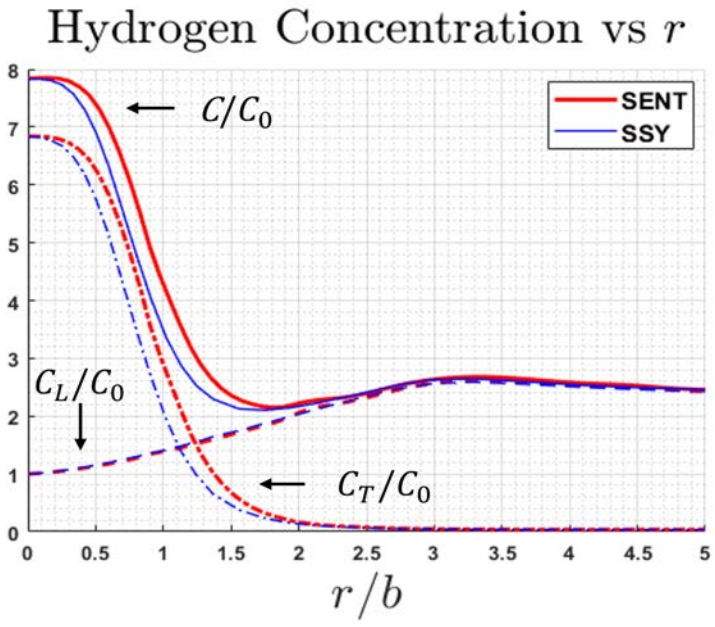

Figure 2.17: The magnitudes of $\frac{C_L}{C_0}$, $\frac{C_T}{C_0}$ and $\frac{C}{C_0}$ are compared in steady state for the SENT specimen and the boundary layer formulation.

In order to better understand how the hydrogen concentration in NILS progresses through time, estimations were made in different time moments, near the crack tip both for the SENT specimen and SSY formulation. It was observed that steady state was reached almost after 30 minutes. The comparison of the NILS concentration in the SENT specimen and the boundary layer formulation for different time moments can be seen in Fig. 2.18a and 2.18b.

Figure 2.18 shows that by considering hydrogen diffusion through the crack face, more

hydrogen is diffused through the metal's lattice as time passes until steady state. The numerical results from both for the SENT specimen and SSY formulation simulations are nearly identical.

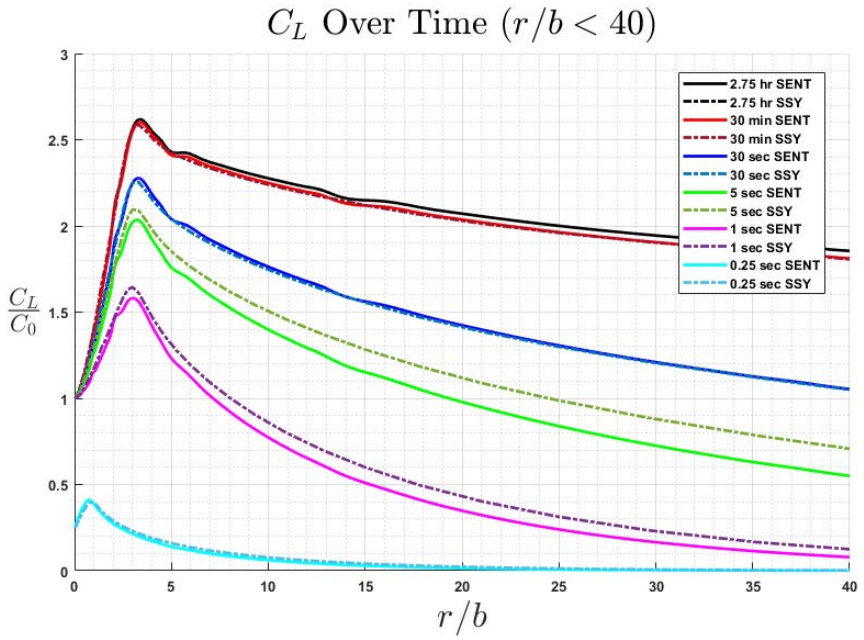

(a)

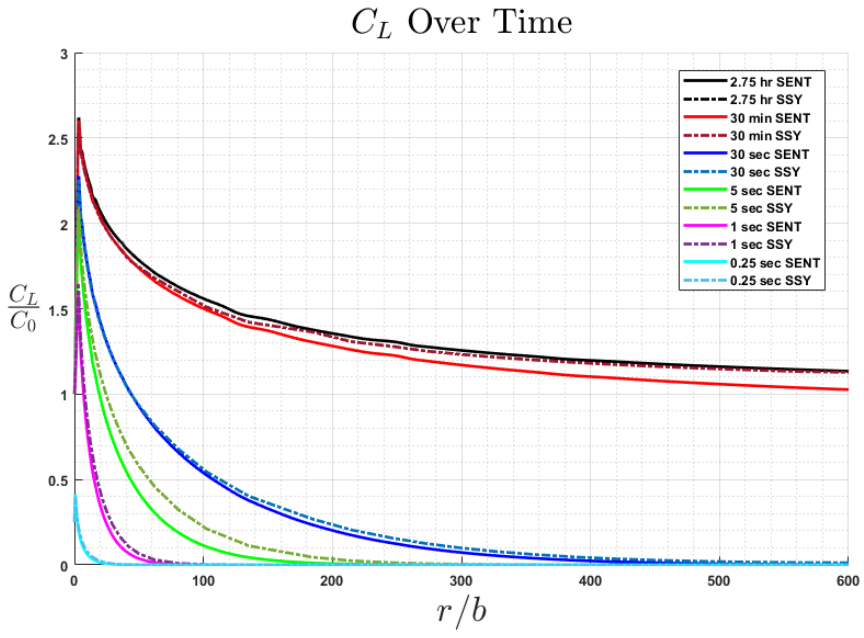

(b)

Figure 2.18: Hydrogen concentration in NILS during different moments in time along the symmetry plane (a) near the crack tip for $r/b < 40$ and (b) along the whole symmetry plane of the SSY formulation.

It can be observed that in all cases, C_L reaches the maximum magnitude at the same distance from the crack tip, at $\frac{r}{b} = 3$ and as the simulation progresses over time, its values

are progressively greater.

Next, the contour plots of the hydrogen concentration fields were extracted, in order to visualize them and obtain a better understanding. At the present work, the subject of interest is the boundary layer formulation.

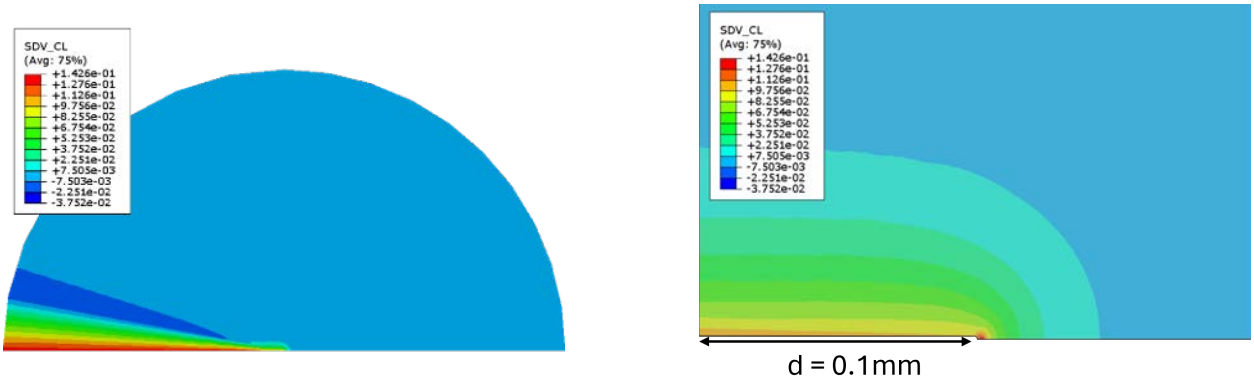

(a) (b)

Figure 2.19: C_L concentration in 0.1 seconds (a) in the full boundary layer formulation domain and (b) closer to the crack tip.

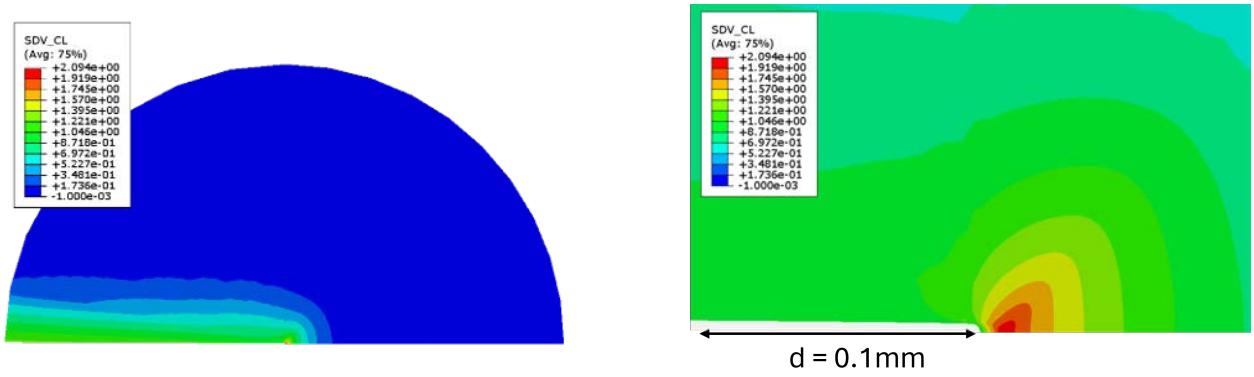

(a) (b)

Figure 2.20: C_L concentration in 5 seconds(a) in the full boundary layer formulation domain and (b) closer to the crack tip.

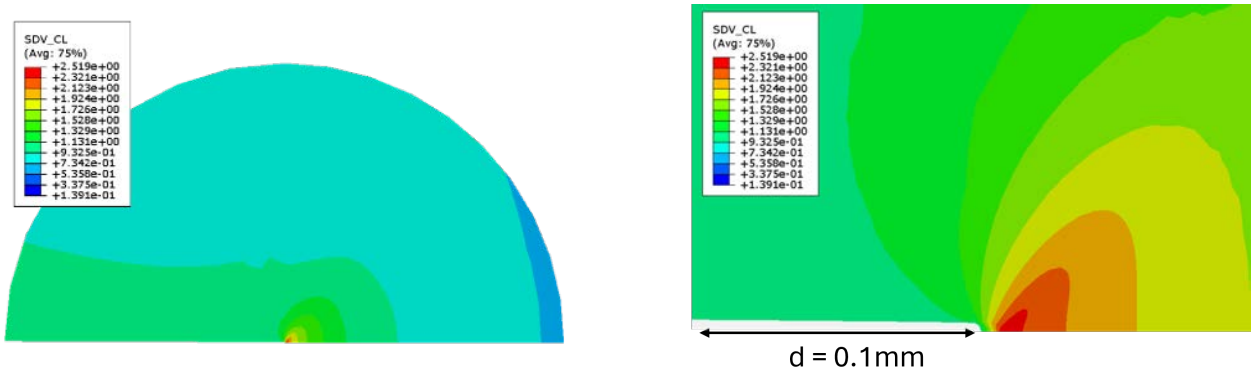

(a) (b)

Figure 2.21: C_L concentration in 5 minutes(a) in the full boundary layer formulation domain and (b) closer to the crack tip.

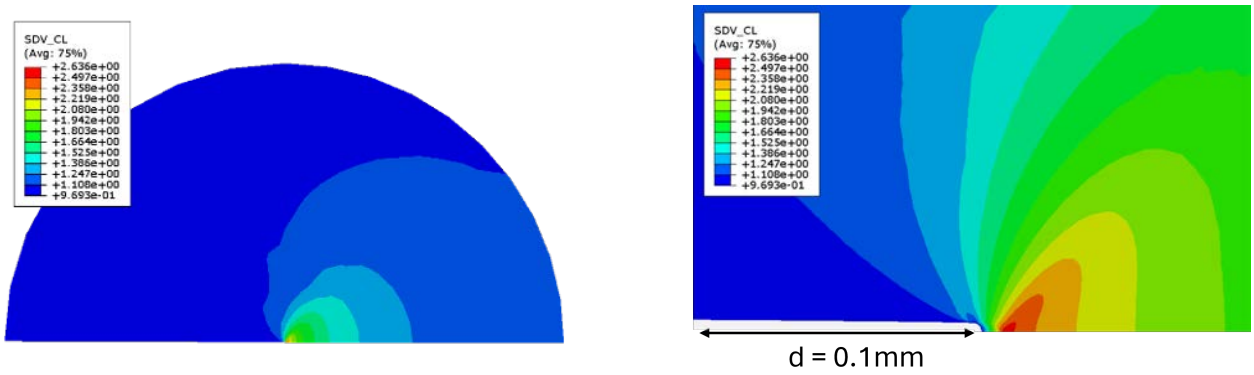

(a) (b)

Figure 2.22: C_L concentration in 1 hour(a) in the full boundary layer formulation domain and (b) closer to the crack tip.

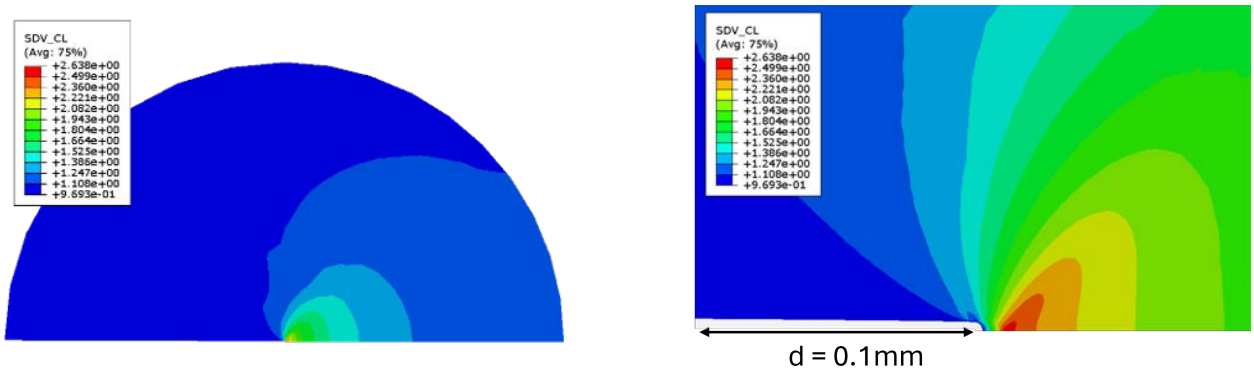

(a) (b)

Figure 2.23: C_L concentration in Steady State(a) in the full boundary layer formulation domain and (b) closer to the crack tip.

In the last part of this work, the influence of loading rate to the hydrogen concentration solutions was investigated, since due to one way coupling and the fact that hydrogen diffusion is a rate-dependant phenomena, it was expected that the hydrogen concentration fields will be influenced from the rate the mechanical loads are being applied. The fields of C_L, C_T and C were evaluated for the occasions where the mechanical load is being applied linearly in 1 minute, 10 minutes and 1 hour respectively and the numerical results are respectively depicted with red, green and a blue curve.

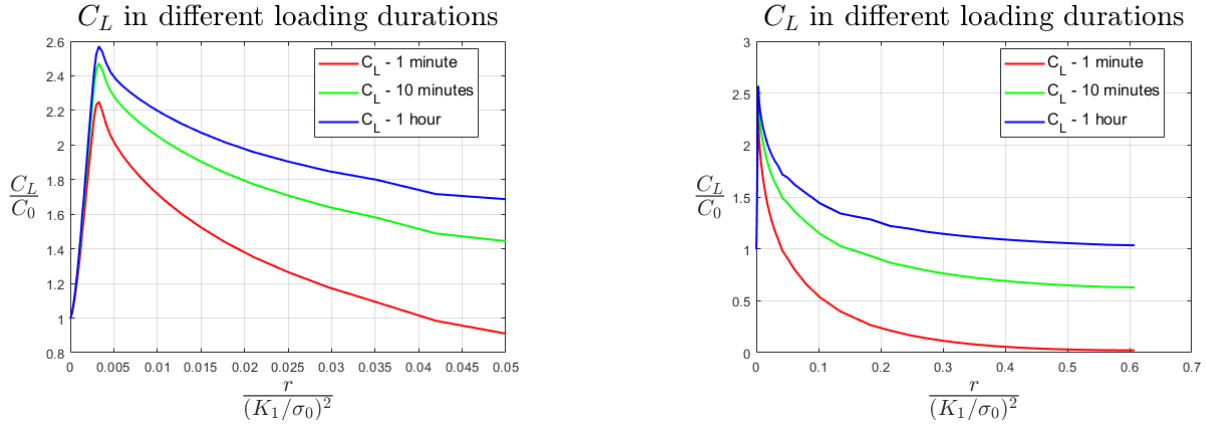

Figure 2.24: NILS hydrogen concentration C_L/C_0 (a) near the crack tip and (b) in full domain.

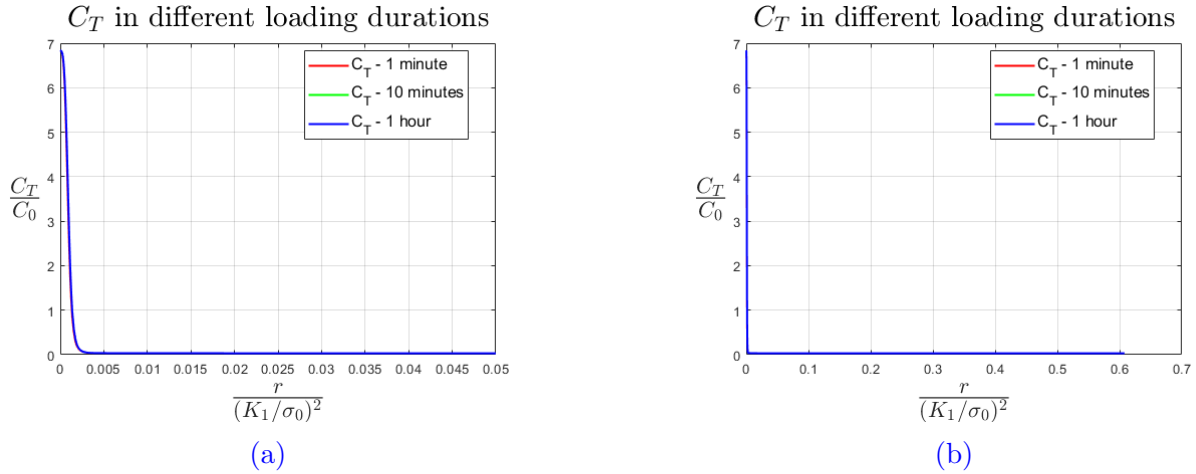

Figure 2.25: Hydrogen concentration in trapping sites C_T/C_0 (a) near the crack tip and (b) in full domain.

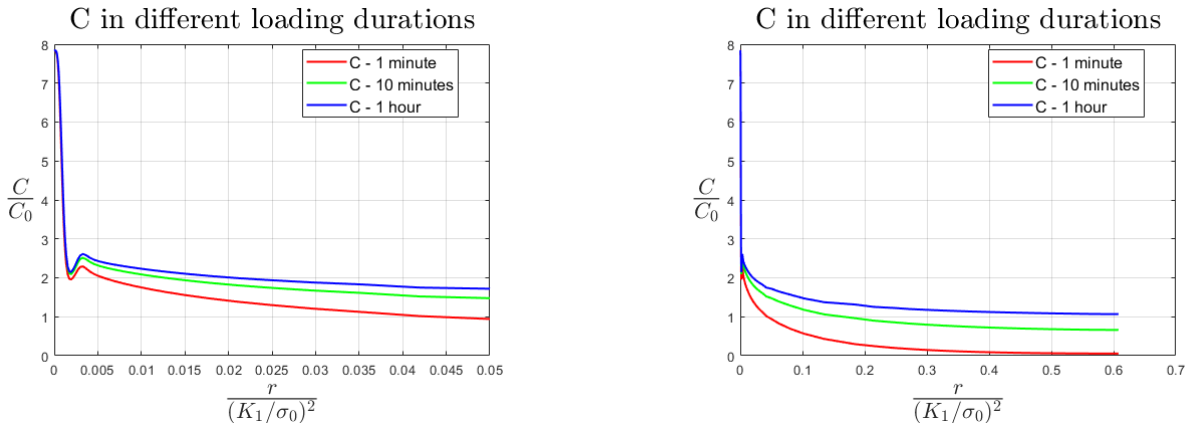

(a) (b)

Figure 2.26: Total hydrogen concentration C/C_0 (a) near the crack tip and (b) in full domain.

It can be seen from the Fig 2.24 - 2.26, that the duration at which the mechanical load is being applied, indeed influences the hydrogen concentration fields. At the crack tip, the C_L/C_0 is the same due to boundary conditions and since the stress fields are the same no matter the loading duration, the final equivalent plastic strain is the same. Noticing Fig. 1.1 and 2.8, the equivalent plastic strain in the simulations at the crack tip corresponds to a constant value of N_T, leading to a common magnitude for C_T at the crack tip. Also, since saturation of the trapping sites occurs due to plasticity, there are no free trapping sites and the hydrogen atoms migrate in the lattice through the NILS. This can be observed in Fig. 2.24b and 2.25b, since at the same length when $C_T = Constant$, the magnitude of C_L reaches its maximum value.

Conclusions

In this work a modified boundary layer formulation, [8], was used in order to investigate the mechanical fields and hydrogen distribution developing near the crack tip of a SENT specimen. Firstly, by applying Kumnick and Johnson's suggestion, a function between the trap density N_T and equivalent plastic strain $\bar{\varepsilon}^p$ a trap saturation point is used. Next, in order to relate C_L and C_T with a rate dependent equation, the relation suggested by McNabb and Foster is being utilized. Then, before analysing the mechanical constitutive equations that characterise the elastoplastic behaviour of the material, the hydrogen diffusion is expressed through the mass conservation equation. Some aspects of Fracture Mechanics were used and modified accordingly, since the pressure applied at the crack surface had to be taken into consideration. Next, the model was set and used. The boundary and initial conditions were chosen and applied based on hydrogen concentration equilibrium as suggested by Sieverts law. Before finalising and meshing the boundary formulation domain, the heat-mass transfer analogy was expressed by using the energy balance equation.

When the SSY hypothesis with a modified boundary formulation was compared to the SENT specimen analysis, some important observation could be done. Firstly, the hypothesis of this work is fully defined when both the K_I and T-stress terms are used to express the boundary layer formulation. Also, the stress fields when estimated numerically, had the tendency of approaching the asymptotic solution defined by both the first and second term. The numerical results in steady state, regarding either the mechanical fields (σ_{11}, σ_{22}, p/σ_0, $\bar{\varepsilon}^p$) or the hydrogen concentration fields (C_L,C_T,C) are in a quite sufficient agreement, meaning that the initial hypothesis of approaching the SENT specimen as a modified boundary formulation near the crack tip was reasonable. Also, based on the time span the mechanical was applied, the hydrogen fields were indeed influenced, as expected due to hydrogen diffusion being a rate-dependant phenomena.

The present work can be extended in several directions. For instance, the effect of hydrogen on the mechanical response could be considered by carrying out fully coupled numerical simulations. Finally, the effect of hydrogen on damage and the comparison with available experimental results could be explored by using an explicit solver such as ABAQUS/Explicit.

Bibliography

[1] Xing, X., Zhou, J., Zhang, S., Zhang, H., Li, Z., & Li, Z. (2019). Quantification of temperature dependence of hydrogen embrittlement in pipeline steel. *Materials*, *12*(4), 585.

[2] Yang, K., Tao, X., Zeng, Z., & Wang, X. (2023). Effects of pressure on hydrogen diffusion behaviors in MgO. *Physical Chemistry Chemical Physics*, *25*, 19824–19833.

[3] Dwivedi, S. K., & Vishwakarma, M. (2018). Hydrogen embrittlement in different materials: A review. *International Journal of Hydrogen Energy*, *43*(46), 21603–21616.

[4] Lee, J. A., & Woods, S. (2016). Hydrogen embrittlement.

[5] Cotterill, P. (1961). The hydrogen embrittlement of metals. *Progress in Materials Science*, *9*(4), 205–301.

[6] Dadfarnia, M., Somerday, B. P., Sofronis, P., Robertson, I. M., & Stalheim, D. (2009). Interaction of hydrogen transport and material elastoplasticity in pipeline steels.

[7] Dadfarnia, M., Sofronis, P., Somerday, B. P., Balch, D. K., Schembri, P., & Melcher, R. (2011). On the environmental similitude for fracture in the SENT specimen and a cracked hydrogen gas pipeline. *Engineering Fracture Mechanics*, *78*(12), 2429–2438.

[8] Dadfarnia, M., Sofronis, P., Somerday, B. P., & Robertson, I. M. (2008). On the small scale character of the stress and hydrogen concentration fields at the tip of an axial crack in steel pipeline: effect of hydrogen-induced softening on void growth. *International Journal of Materials Research*, *99*(5), 557–570.

[9] Crank, J. (1979). *The mathematics of diffusion*. Oxford University Press.

[10] Hashim, F. A., Mostafa, R. R., Hussien, A. G., Mirjalili, S., & Sallam, K. M. (2023). Fick's Law Algorithm: A physical law-based algorithm for numerical optimization. *Knowledge-Based Systems*, *260*, 110146.

[11] Oriani, R. A. (1970). The diffusion and trapping of hydrogen in steel. *Acta Metallurgica*, *18*(1), 147–157.

[12] Wert, C. A. (1978). Trapping of hydrogen in metals. In *Hydrogen in Metals II: Application-Oriented Properties*, 305–330.

[13] Pressouyre, G. M. (1980). Trap theory of hydrogen embrittlement. *Acta Metallurgica*, *28*(7), 895–911.

[14] Sofronis, P., Liang, Y., & Aravas, N. (2001). Hydrogen induced shear localization of the plastic flow in metals and alloys. *European Journal of Mechanics - A/Solids*, *20*(6), 857–872.

[15] Lubliner, J. (1986). Normality rules in large-deformation plasticity. *Mechanics of Materials*, *5*(1), 29–34.

[16] Sofronis, P., & McMeeking, R. M. (1989). Numerical analysis of hydrogen transport near a blunting crack tip. *Journal of the Mechanics and Physics of Solids*, *37*(3), 317–350.

[17] McNabb, A., & Foster, P. K. (1963). A new analysis of diffusion of hydrogen in iron and ferritic steels. *Transactions of the Metallurgical Society of AIME*, *227*(3), 618.

[18] Williams, M. L. (1957). On the stress distribution at the base of a stationary crack. *Journal of Applied Mechanics*, **24**(1), 109–114.

[19] Christopher, C. J., James, M. N., Patterson, E. A., & Tee, K. F. (2007). Towards a new model of crack tip stress fields. *International Journal of Fracture*, **148**, 361–371.

[20] Vadrucci, M., Borgognoni, F., Moriani, A., Santucci, A., & Tosti, S. (2013). Hydrogen permeation through Pd–Ag membranes: surface effects and Sieverts' law. *International Journal of Hydrogen Energy*, **38**(10), 4144–4152.

[21] Kumnick, A. J., & Johnson, H. H. (1980). Acta Metallurgica, **28**, 33.

[22] Lewicki, D. G., & Ballarini, R. (1997). Rim thickness effects on gear crack propagation life. *International Journal of Fracture*, **87**, 59–86.

[23] Li, Y., Zhu, L., Zhou, M., Lei, Y., Wang, W., He, Z., & Gao, Z. (2020). Weibull stress solutions for 2D cracks under mode II loading. *International Journal of Fracture*, **225**, 31–45.

[24] Kamoutsis 2025 (thesis in progress).

[25] Barrera, O., Tarleton, E., Tang, H. W., & Cocks, A. C. F. (2016). Modelling the coupling between hydrogen diffusion and the mechanical behaviour of metals. *Computational Materials Science*, *122*, 219–228.

[26] Sofronis, P., & McMeeking, R. M. (1989). Numerical analysis of hydrogen transport near a blunting crack tip. *Journal of the Mechanics and Physics of Solids*, *37*(3), 317–350.

.